

Numerical Simulations of Internal Gravity Wave Breaking in the Middle Atmosphere: The Influence of Dispersion and Three-Dimensionalization

YA. D. AFANASYEV* AND W. R. PELTIER

Department of Physics, University of Toronto, Toronto, Ontario, Canada

(Manuscript received 19 April 1999, in final form 9 February 2000)

ABSTRACT

A series of new analyses of the problem of the evolution of the internal gravity wave field that is excited when a uniformly stratified fluid flows over monochromatic topography is presented. Results demonstrate that upward-propagating waves overturn and break when they reach sufficient amplitude. The breaking of the wave field may occur due to either one or the other of two main effects, namely, the instability of the propagating wave front and the instability of the wave established behind the advancing front. The analysis of the wave-mean flow momentum transfer process reveals significant differences between these results and the predictions of two main gravity wave drag parameterization schemes (viz., those based upon so-called saturation theory and the spectral theory based on the critical layer absorption mechanism) regarding the dynamics of wave breaking and the spatial distribution of the resulting momentum transfer. The vertical extent and structure of the breaking region and, hence, the momentum transfer from the wave field to the mean flow, are shown to be highly sensitive to the governing parameter aN/U (U and N are, respectively, the velocity and buoyancy frequency characteristic of the upstream incident flow, while a is the wavelength of a quasi-topographic forcing). This nondimensional parameter provides a measure of the importance of nonhydrostatic effects. When the flow is allowed to access the third spatial dimension, the simulations demonstrate that it develops intense three-dimensional motions in the regions of wave breaking. An instability first appears in the form of streamwise-oriented vortices of alternating sign that are consistent with typical convective instability patterns observed previously by different authors. It was observed, however, that two-dimensional coherence of the main flow is still maintained at the coarse-grain scale although the instability does lead to the onset of small-scale turbulence.

1. Introduction

It is well understood that the breaking of upward propagating internal waves, which occurs when the waves achieve such large amplitude that they are able to invert the local density stratification of the medium through which they propagate, is a dynamically important interaction in the atmosphere and almost certainly also in the oceans. The transfer of momentum from the wave field to the mean flow associated with such internal wave breaking involves not only local mixing of the density field but also a marked impact on the vertical variations of horizontal velocity. The global impact of the wave drag that is a consequence of this momentum transfer is inferred on the basis of a reversed meridional gradient of zonally averaged temperature in the meso-

sphere (e.g., Lindzen 1968) as well as in a limiting of the amplitude of the diabatically forced mesospheric zonal circulation (Lindzen 1981). Seen from this perspective, the accurate representation of the momentum flux associated with upward propagating internal waves is also a key issue in the design of “subgrid” parameterizations for general circulation models [for an extensive recent review of the parameterization problem see Hamilton (1999)]. One may distinguish two basic approaches to the parameterization problem. The first is based on the dynamical processes that occur at critical levels, where the horizontal phase speed of a wave, c , is equal to the mean horizontal wind speed, that is, $c = U(z)$ with U the mean horizontal speed of the flow at height z . It is well understood that there is an increased convergence of the vertical flux of horizontal momentum associated with the wave field near such critical levels. Each component of the wave spectrum transfers its momentum to the mean flow when and where it becomes critical. The nonlinear interactions among components of the wave spectrum can be taken into account together with the background wind to define the levels that are critical to any specific component of an incident spectrum of waves (Hines 1997). Hines’s approach includes the effects of the Doppler shifting of

* Current affiliation: Department of Physics and Physical Oceanography, Memorial University of Newfoundland, St. John’s, Newfoundland, Canada.

Corresponding author address: W. R. Peltier, Department of Physics, University of Toronto, Toronto, ON M5S 1A7, Canada.
E-mail: peltier@atmos.physics.utoronto.ca

waves by the winds associated with the rest of the spectrum. Another approach to gravity wave drag parameterizations is based on the so-called saturation hypothesis (Lindzen 1981). This has been implemented in a number of different general circulation models (e.g., McFarlane 1987; Holton 1982). From the perspective of the saturation hypothesis, wave amplitude is constrained by the requirement that it not be greater than that required to induce neutral stability at the lowest breaking level and is thereafter limited at higher elevations to the saturation value by a turbulent eddy diffusivity to be associated with the turbulence created by the breaking wave itself. In the present paper we will for the most part investigate the simplest possible circumstance in which gravity wave drag arises, namely, that involving monochromatic waves in a uniform mean wind (though some examples of breaking induced by wave packets consisting of superpositions of waves will also be discussed). A goal of the work to be reported herein will be to provide a test of the saturation hypothesis by fully resolving the hydrodynamic interactions that ensue when waves break.

A very large number of recent theoretical studies have led to the suggestion of a variety of possible instabilities that might mediate the wave–mean flow interaction induced by wave breaking under different circumstances (see, e.g., Hines 1971; Fritts and Rastogi 1985; Dunkerton 1987; Klostermeyer 1991). A simplified classification of possible gravity wave instabilities was recently proposed by Sonmor and Klaassen (1997) on the basis of numerical linear stability analysis. Their approach relies upon the validity of the assumption that typical timescales of the instability and background flow evolution are widely separated and, hence, that the wavy basic state can be considered steady for the purpose of the stability analysis. In physical reality these timescales are of course often comparable. It is therefore rather clear that the development of internal wave instabilities should be considered together with the evolution of the parent wave and therefore direct numerical simulations of this unsteady nonlinear process are necessary in developing a realistic picture of wave breaking. Such simulations turn out to be rather challenging, however, in terms of the computational resources required, since most instabilities are essentially three-dimensional and the associated small-scale motions should be resolved in a deep computational domain that enables simulation of the entire process of wave field evolution with height. In the present paper we will focus on the waves propagating initially in a shearfree environment, rather than the waves interacting with background shear, which has been the focus of extensive recent studies by Andreassen et al. (1994), Winters and D’Asaro (1994), Fritts et al. (1996), Andreassen et al. (1998), Fritts et al. (1998), and Dornbrack (1998).

The main purpose of this paper is to more fully elucidate a number of basic dynamical features of the wave breaking process and their effects upon the basic state

of the flow for a range of values of the control parameters in a specially designed series of two- and three-dimensional numerical simulations. If the incident flow has uniform velocity profile (U) and constant buoyancy frequency (N), then dimensional analysis (e.g., Afanasyev and Peltier 1998) requires the flow to be governed by three appropriately defined nondimensional parameters, namely,

$$F_v = \frac{hN}{U}, \quad F_h = \frac{aN}{U}, \quad F_\rho = \frac{HN}{U}.$$

These nondimensional parameters represent the ratios of different length scales (viz., height h , and wavelength a of the (quasi) topography and density scale height H) to the intrinsic vertical length scale of the flow U/N , which is also the inverse vertical wavenumber of stationary hydrostatic internal waves. The nondimensional parameter F_v is a measure of the degree of nonlinearity (due to the finite-amplitude lower boundary condition) to be expected of the flow. The second nondimensional parameter F_h provides a measure of the importance of nonhydrostatic effects. The inverse value of this parameter multiplied by 2π gives the angle ϕ between the vertical and wave crests (e.g., Gill 1982), such that

$$\cos\phi = \frac{2\pi}{F_h} = \frac{Uk_x}{N}.$$

Here $k_x = 2\pi/a$ is the horizontal wavenumber of the waves generated by the (quasi) topography of wavelength a . Both F_v and F_h govern the dynamics of breaking of upward-propagating internal waves. When F_v is large enough and F_h is not especially small [see, e.g., the regime diagram in Fig. 2 in Afanasyev and Peltier (1998)] wave breaking may occur at a low level, within one vertical wavelength of the surface. In the case of localized topography and for such values of these parameters, the interesting phenomenon of severe downslope windstorm formation occurs and has been observed in nature and extensively studied both numerically and theoretically (see, e.g., Peltier and Clark 1979, 1983; Smith 1985; Durran 1986; Scinocca and Peltier 1989; Laprise and Peltier 1989a,b; Afanasyev and Peltier 1998). In the opposite case, when F_v is small, breaking begins far from the surface and it is this regime that will be of interest to us herein. The third nondimensional parameter, $F_\rho = HN/U \propto g/NU$, measures the importance of non-Boussinesq effects. It was shown in our recent study (Afanasyev and Peltier 1998) that these effects can be a significant factor in the dynamics of severe downslope windstorms; in fact, they are determinant of the intensity of the Kelvin–Helmholtz instability induced pulsations that control the strength of the transience that is characteristic of the fully developed flow.

The present study will be focused on the regime in which the waves break in the middle atmosphere (F_v is small) and non-Boussinesq effects might be important.

The values $F_v = 0.21$ and $F_\rho = 10$ will be fixed in the sequence of numerical experiments that we intend to describe, while the value of ϕ (and hence F_h) will be varied in the range $\phi = 10^\circ$ – 70° . Thus, nonhydrostatic waves (small “takeoff” angles) in which fluid particles oscillate almost vertically as well as almost hydrostatic waves (large takeoff angles) in which fluid parcels oscillate almost horizontally will be considered.

A few relatively recent numerical studies of upward-propagating gravity waves have revealed several properties of the wave breaking events that are expected in such circumstances. Two-dimensional numerical simulations of hydrostatic monochromatic gravity waves performed by Walterscheid and Schubert (1990), in particular, demonstrated that the breakdown of the wave occurred as a consequence of convective instability driven by the unstable density gradients established by wave overturning. More recent simulations of waves excited by a localized mountain in two space dimensions (Prusa et al. 1996) and in three dimensions (Prusa et al. 1997) have demonstrated that the waves break in a deep region and that the altitude of the upper boundary of the breaking region is governed by the parameters of sponge-layer damping employed in the numerical model, while the amplitude of forcing has little effect on the highest altitude at which breaking occurs. However, since an entire spectrum of waves with different horizontal wavenumbers and different frequencies (since the amplitude of the topography was time dependent) was excited and then analyzed, it is hard to acquire insight concerning the behavior of a wave in the more idealized circumstances that we will describe herein, when the forcing is both monochromatic in time and periodic in the horizontal direction. The latter authors (Prusa et al. 1997) also mentioned that in their three-dimensional simulations they observed the development of a spanwise instability of the overturning wave, though the period of growth of the instability was limited and its intensity was not sufficient to make the flow significantly three-dimensional. The development of secondary three-dimensional instability is a typical feature of the flow when overturning motions of any nature occur in a stratified fluid (see, e.g., Thorpe 1985, 1987; Schowalter et al. 1994; Voropayev et al. 1993). The usually dominant three-dimensional shear aligned convective instability that controls the three-dimensionalization process in Kelvin–Helmholtz billows has been extensively studied both theoretically and numerically (Klaassen and Peltier 1985a,b,c; 1989; 1991; Smyth and Peltier 1991, 1993, 1994; Caulfield and Peltier 1994). It is this Klaassen–Peltier (K–P) instability that drives the growth of streamwise longitudinal rolls of alternate vorticity that subsequently lead to the complete turbulent collapse of the billow core. The K–P instability is also responsible for the growth of the streamwise vortices in our recent simulations of downslope windstorms (Afanasyev and Peltier 1998). The results of the latter study have demonstrated that intense three-dimensional motions devel-

op in the regions where overturning of the isentropes in the otherwise stably stratified fluid takes place, namely, in the region of breaking of the wave above the mountain crest and in Kelvin–Helmholtz billows that are themselves a typical feature of downslope windstorms. The three-dimensional convective instability first appears in the form of streamwise-oriented vortices of alternating sign. This instability then erodes the downstream-propagating Kelvin–Helmholtz billows, eventually leading to the complete arrest of their continued propagation as they “dissolve” into fully developed turbulent flow.

An important consideration in numerical (as well as theoretical) analyses is to formulate physically meaningful initial conditions and then to construct an appropriate numerical initialization that is true to them. Since our aim is to study the gravity wave problem in its most simplified form, we will assume that the fluid is impulsively set into motion at $t = 0$ (see, e.g., McIntyre 1972 and section 5.5.1 in Baines 1995). This gives rise to potential (irrotational) flow at $t = 0$, which is described by the Laplace equation for the streamfunction with appropriate boundary conditions. This formulation of the physical problem implies that one can use the potential flow over a given topography for “smooth” startup of numerical calculations in order to avoid nonphysical transients that otherwise occur in “shock” startup (when the flow is initialized without topography and then the topography is suddenly introduced). Another approach to the formulation of the physical problem and hence to the numerical initialization is to gradually increase the height of the topography (e.g., Prusa et al. 1996) or the speed of the background flow. However, in that case the forcing is time dependent and the flow at any given time is the result of all intermediate states of its evolution. Since our aim is to study the simplest possible formulation of the problem in which the main governing parameters of the flow are fixed during flow evolution, we have chosen to employ the impulsive startup procedure for the purpose of the analyses to be reported herein. Impulsive startup can in fact be considered to be a limiting case of very unsteady flow. In this respect some insight into the details of unsteady flow evolution for forced internal wave problems has been provided by Lott and Teitelbaum (1993). These authors studied the waves generated by a time-dependent wind field over sinusoidal topography. In their analysis the wind field was assumed to be characterized by one accelerating phase and one decelerating phase. When temporal variations of the incident wind were rapid compared to the advective timescale, a/U , the disturbance generated by the topography did not have sufficient time to develop as an internal gravity wave during the first accelerating phase. Following this phase, the disturbance was localized near the ground and the vertical scale of the disturbance for the particular case considered by the authors was almost six times

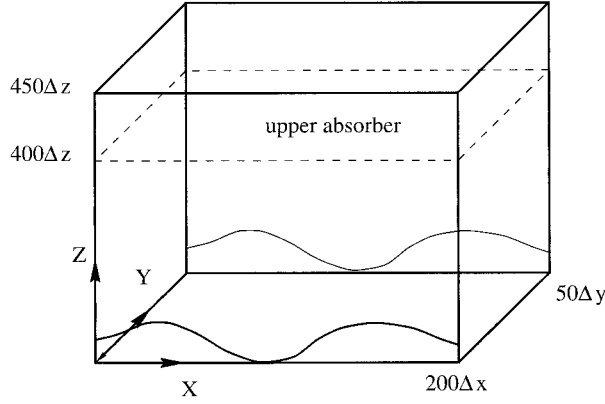


FIG. 1. The model domain.

larger than the characteristic wavelength ($2\pi U/N$) of the related topographically forced internal wave.

In the following sections of this paper, the equations of motion and boundary and initial conditions employed in the numerical model will be discussed. The new sequence of simulations that document flow evolution for different degrees of hydrostaticity in two dimensions as well as the development of instabilities in three dimensions is described and discussed in section 3. Conclusions are offered in section 4.

2. Model equations and boundary and initial conditions

The numerical model to be employed to perform the simulations discussed herein is essentially that described in Clark (1977) and first employed in the context of analyses of topographically forced internal waves in Clark and Peltier (1977). The model is based upon the anelastic approximation to the equations of motion, which may be written in the form

$$\bar{\rho} \frac{du_i}{dt} = -\partial_i p' - \delta_{i3} g \rho' + \partial_j \bar{\rho} K_M D_{ij} \quad (1)$$

$$\partial_i (\bar{\rho} u_i) = 0 \quad (2)$$

$$\bar{\rho} \frac{d\theta}{dt} = \partial_i (\bar{\rho} K_H \partial_i \theta), \quad (3)$$

in which u_i ($i = 1, 2, 3$) are the components of velocity in (x, y, z) Cartesian coordinates, and θ is potential temperature. Here p' and ρ' are pressure and density fluctuations respectively, such that

$$p = \bar{p}(z) + p'(x, y, z, t) \quad (4)$$

$$\rho = \bar{\rho}(z) + \rho'(x, y, z, t) \quad (5)$$

$$\frac{d\bar{p}}{dz} = -\bar{\rho}g. \quad (6)$$

The overbar denotes a hydrostatic background state variable, and the deformation tensor \mathbf{D}_{ij} is given by

$$\mathbf{D}_{ij} = \partial_j u_i + \partial_i u_j - \frac{2}{3} \delta_{ij} \partial_k u_k. \quad (7)$$

The anelastic approximation filters sound waves while allowing for the variation of background density and other thermodynamic fields with height. The connection between the thermodynamic variables p , ρ , θ will be herein assumed to be given by the ideal gas equation of state, namely,

$$p = \rho RT. \quad (8)$$

Our anelastic equations are formulated in terms of potential temperature θ rather than absolute temperature T , the two variables being related by the definition

$$\theta = T \left(\frac{p}{p_0} \right)^{-\kappa}, \quad (9)$$

TABLE 1. Parameters used in two-dimensional numerical experiments.

Experiment	Δx (m)	Nx	Δz (m)	Nz	a (km)	h (m)	ϕ ($^\circ$)
1	23.9	200	66.7	450	4.8	200	10
2	25	200	200	300	5.0	200	19.5
3	25	200	100	300	5.0	200	19.5
4	25	200	70	300	5.0	200	19.5
5	25	200	50	450	5.0	200	19.5
6	28.8	200	111	450	5.75	200	35
7	35.625	200	200	550	7.125	200	49
8	35.625	200	200	550	7.125	400	49
9	35.625	200	200	550	7.125	600	49
10	42	200	300	300	8.4	200	56
11	42	200	200	250	8.4	200	56
12	42	200	125	400	8.4	200	56
13	68.9	200	200	450	13.8	200	70
14	71.25	200	200	550	14.25	200	71
15	71.25	200	200	550	14.25 (1, 1/2, 1/3)	200 (1/3, 1/3, 1/3)	71, 49, 7
16	71.25	200	200	550	14.24 (1, 1/2, 1/3)	200 (1, 2/3, 1/3)	71, 49, 7
17	215.325	200	200	550	43.065 (1, 1/3)	200 (1, 1/3)	84, 10
18	215.325	200	200	550	43.065 (1, 1/3)	200 (1, 1/2)	84, 10

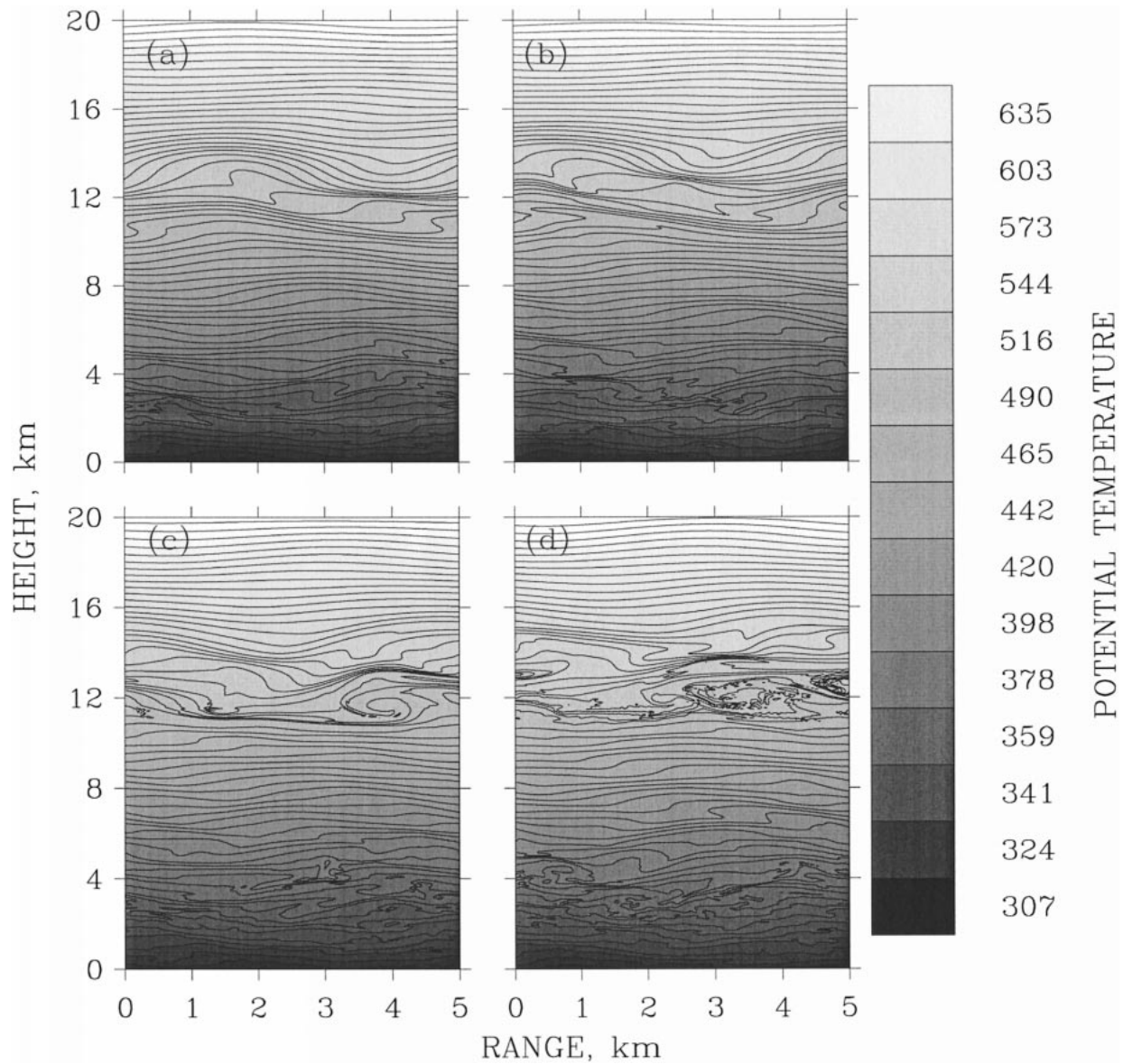


FIG. 2. Contour plots of potential temperature for the simulation with $\phi = 19.5^\circ$ (expt 5 in Table 1), (a) $t = 55$, (b) 57.5, (c) 60, (d) 62.5 min.

in which p_0 is the surface pressure at $z = 0$, and $\kappa = R/C_p = 0.286$ for dry air.

A linearization of (8) and (9) results in

$$\rho' = \frac{p'}{\gamma RT} - \bar{\rho} \frac{\theta'}{\theta}, \quad (10)$$

in which $\gamma = C_p/C_v$ is the usual ratio of specific heats. We employed uniform viscosity $K_M = 0.5\text{--}50 \text{ m}^2 \text{ s}^{-1}$ as well as a nonuniform viscosity distribution given by the first order closure (Lilly 1962):

$$K_M = \begin{cases} (c\Delta)^2 |\text{def}| (1 - \text{Ri})^{1/2}, & \text{if } \text{Ri} \leq 1; \\ 0, & \text{otherwise.} \end{cases} \quad (11)$$

In (11) $c = 0.23$ is a numerical constant, Δ is a measure of the grid resolution [for the two-dimensional case $\Delta = (\Delta x \Delta z)^{1/2}$ and for the three-dimensional case $\Delta = (\Delta x \Delta z \Delta y)^{1/3}$], and Ri is the local gradient Richardson number

$$\text{Ri} = g \frac{d \ln \theta}{dz} (\text{def})^{-2}, \quad (12)$$

in which the total deformation def is defined as

$$(\text{def})^2 = \frac{1}{2} \sum_i \sum_j D_{ij}^2. \quad (13)$$

The first-order closure (11) for the mixing coefficient

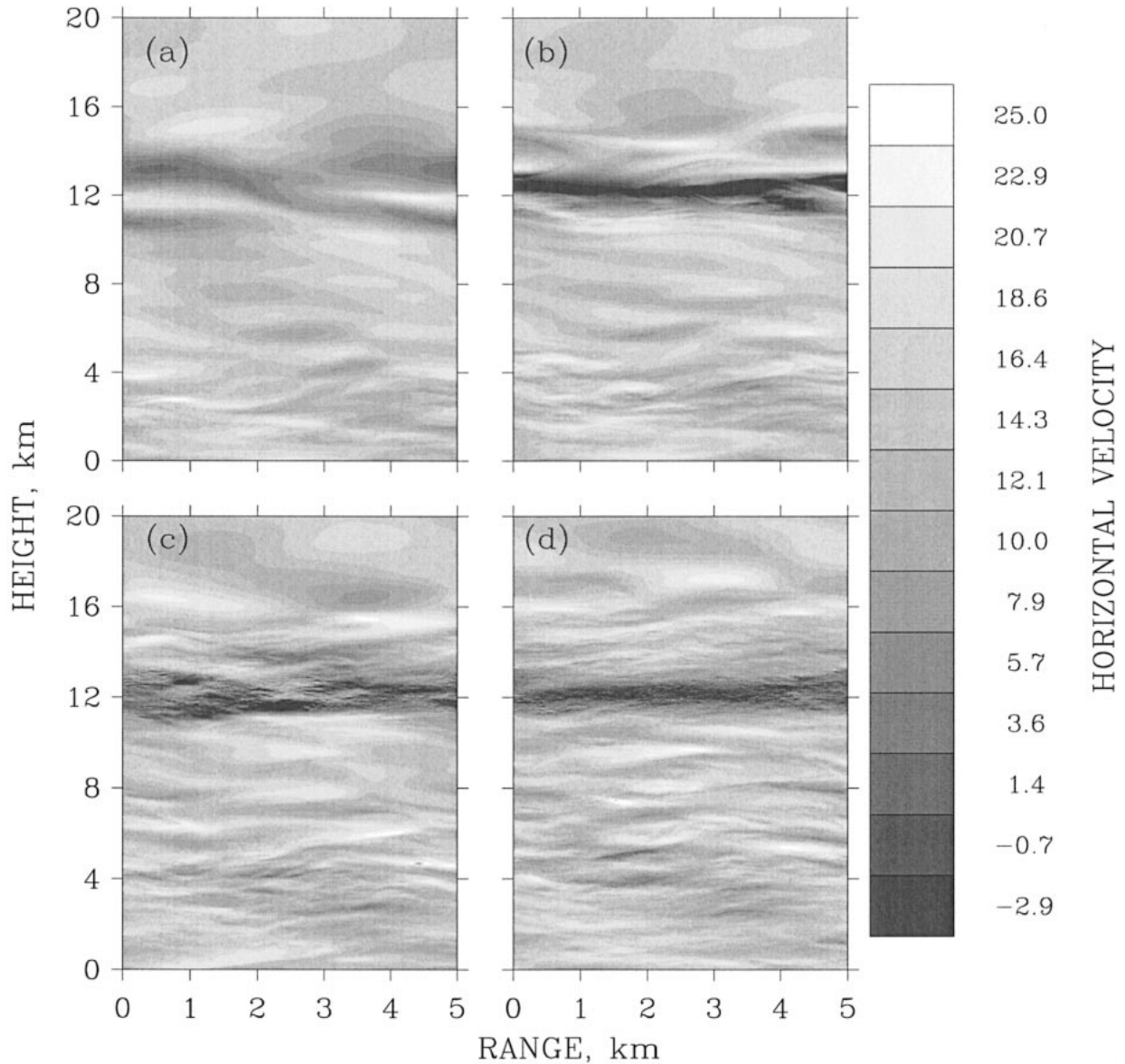


FIG. 3. Contour plots of horizontal velocity (u_x) for the simulation with $\phi = 19.5^\circ$ (expt 5 in Table 1), (a) $t = 55$, (b) 62.5, (c) 70, (d) 77.5 min.

for momentum enhances viscous dissipation where the motion becomes sufficiently complicated that the scale of the grid can no longer resolve it, while leaving the rest of the flow domain effectively inviscid. The mixing coefficient for heat, K_H , is taken to be equal to K_M so that the Prandtl number $\text{Pr} = K_M/K_H$ is unity.

In Fig. 1 we present a schematic of the model domain to be employed for the purpose of the three-dimensional calculations to be discussed in what follows. For the initial two-dimensional integrations the XZ section of the domain is employed. At the inflow and outflow boundaries periodic boundary conditions are applied while a rigid-lid condition is imposed on the upper horizontal boundary of the model. In order to simulate an

unbounded fluid, an absorbing region (with enhanced friction) is employed near the top of the model domain. This is introduced to prevent the reflection of internal waves that are incident upon the upper boundary from below. The topography (h_s) used in most of the simulations is two-dimensional and of the simple sinusoidal form

$$h_s(x) = h \left[1 + \sin\left(\frac{2\pi x}{a}\right) \right], \quad (14)$$

in which h is the height of the topography and a is its wavelength. The parameter h is kept to the constant

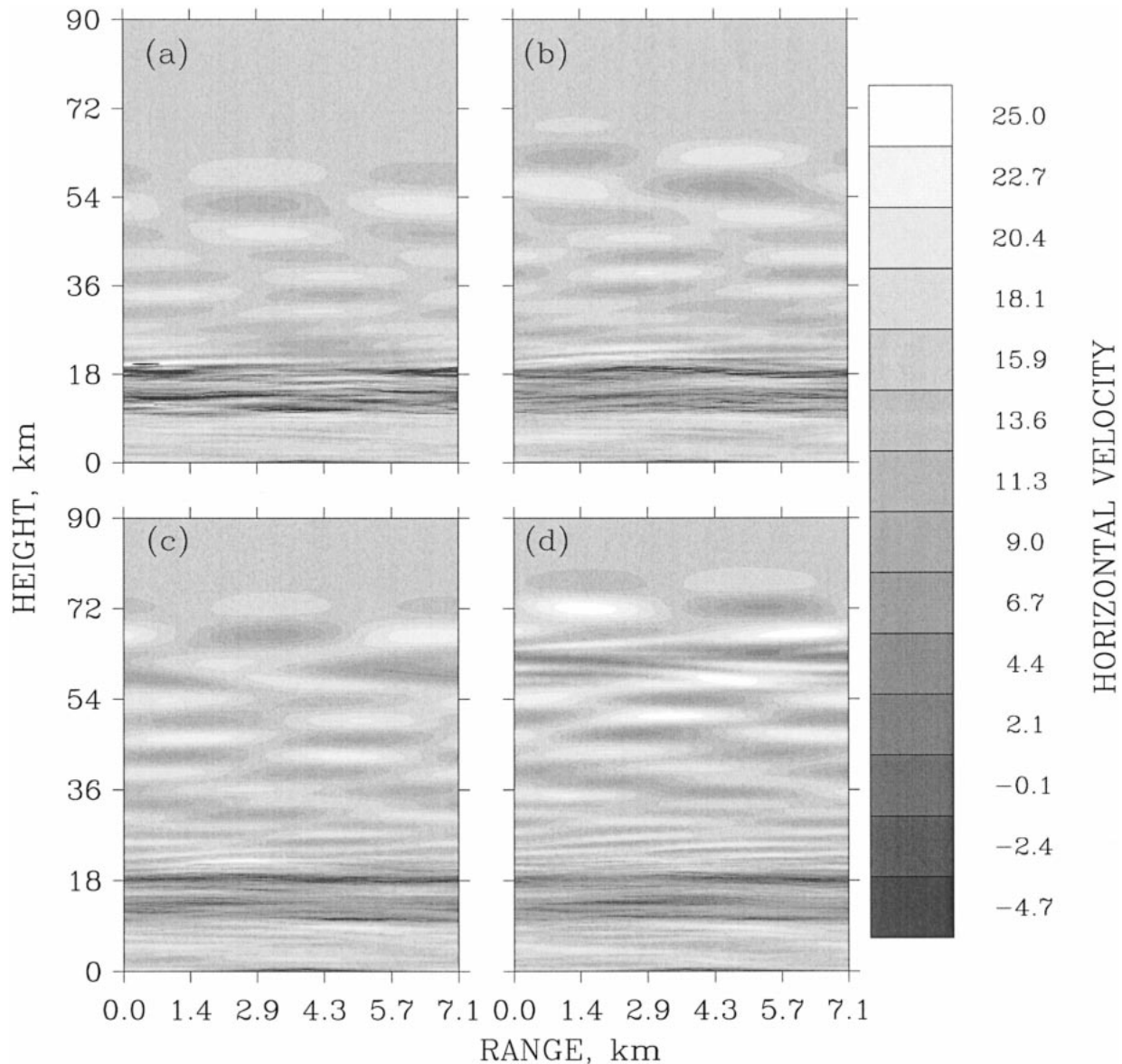


FIG. 4. Contour plots of horizontal velocity (u_x) for the simulation with $\phi = 49^\circ$ (expt 7 in Table 1), (a) $t = 70$, (b) 80, (c) 90, (d) 100 min.

value $h = 0.2$ km while a is varied through the range $a = 5\text{--}14$ km between different experiments.

Four simulations were performed for topography presented by the sum of two or three waves:

$$h_s(x) = \sum_{i=1}^n h_i \left[1 + \sin\left(\frac{2\pi x}{a_i} + \alpha_i\right) \right], \quad n = 2, 3,$$

with random phases (α_i) and different wavelengths [e.g., $a = 14.25(1, \frac{1}{2}, \frac{1}{3})$ km]. Thus the periodic boundary conditions were satisfied for all waves in the computational domain of length equal to the wavelength of the longest wave. The wave amplitudes were either taken to be equal each other [e.g., $h = 200(\frac{1}{3}, \frac{1}{3}, \frac{1}{3})$ m] or were varied with

wavelength [e.g., $h = 200(1, \frac{2}{3}, \frac{1}{3})$ m] to approximate either a white or a red spectrum, respectively.

In all of the experiments to be discussed in the present paper, the upstream profiles of u and θ will be assumed to be given by

$$\bar{u} = U = \text{const} \tag{15}$$

$$\bar{\theta} = \theta_0 \exp\left(\frac{zN^2}{g}\right), \tag{16}$$

from which the buoyancy frequency N may be determined as

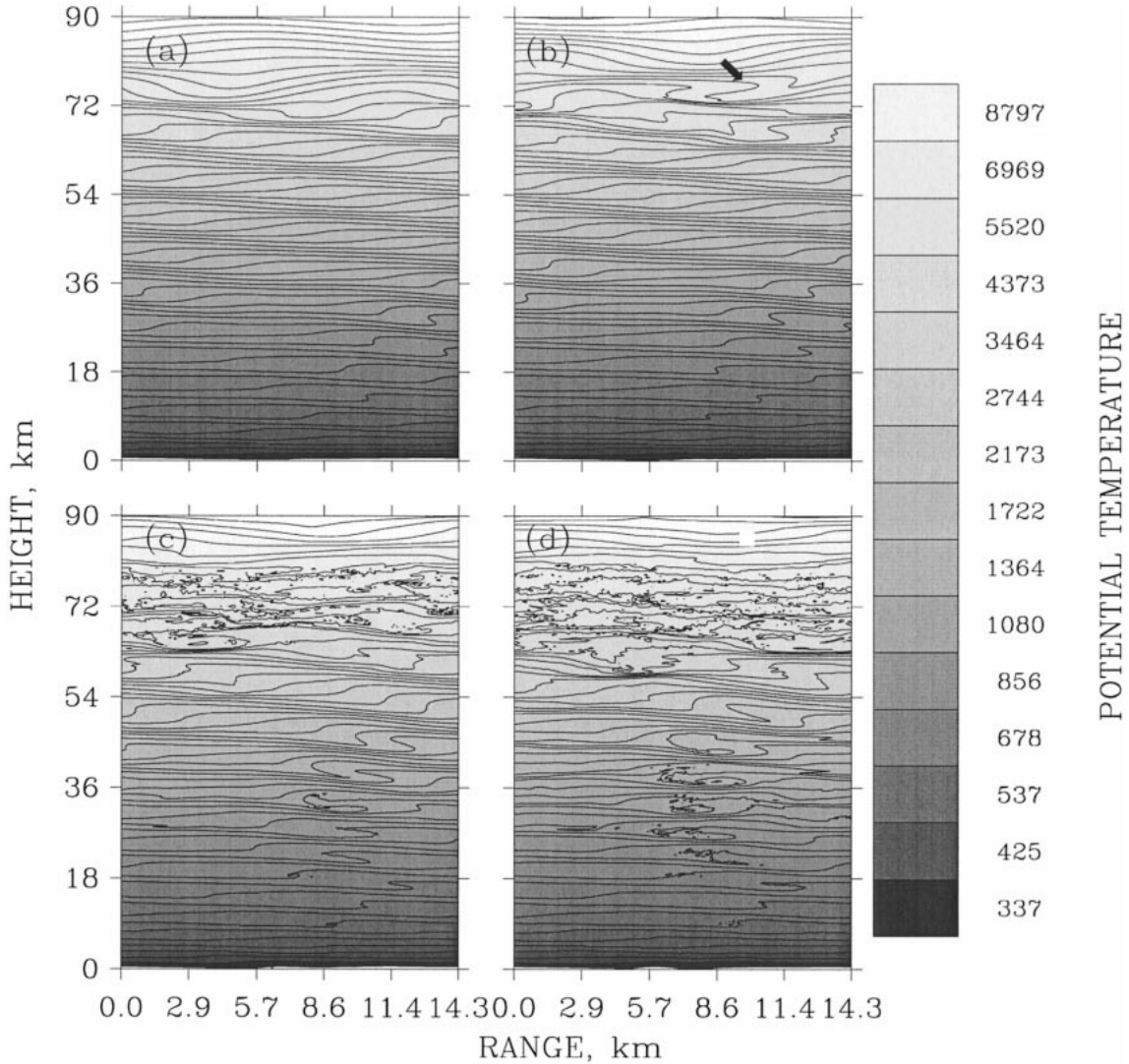


FIG. 5. Contour plots of potential temperature for the simulation with $\phi = 71^\circ$ (expt 14 in Table 1), (a) $t = 80$, (b) 85, (c) 95, (d) 100 min. An arrow shows a typical S-shaped feature of the unstable wave front where the wave overturns clockwise.

$$N^2 = \frac{g}{\theta} \frac{d\bar{\theta}}{dz}, \quad (17)$$

The background velocity $U = 15 \text{ m s}^{-1}$ and $N = \text{constant} = 0.02 \text{ s}^{-1}$ will be fixed in the sequence of experiments that we intend to describe. The background density in the anelastic basic state then has the simple analytic form

$$\bar{\rho}(z) = \rho_0 \exp\left(-\frac{z}{H}\right), \quad (18)$$

in which the density scale height H is related to the buoyancy frequency through the relationship

$$H = \kappa \frac{g}{N^2} \approx 7.1 \text{ km}. \quad (19)$$

The three-dimensional calculations are initialized from

the two-dimensional calculations. For the purpose of these analyses, the flow is allowed to develop in three dimensions only after some period of two-dimensional evolution. This was done to avoid the introduction of possibly spurious three-dimensional effects due to the starting transient and also to conserve computational resources, since the three-dimensional calculations are extremely expensive both in terms of CPU time and memory. The analyses that we will report herein have all been performed on the Cray J916 computer system in our laboratory in Toronto.

3. Results and interpretation of two- and three-dimensional simulations

In what is to follow we will focus successively upon the detailed processes involved in the breaking of two-

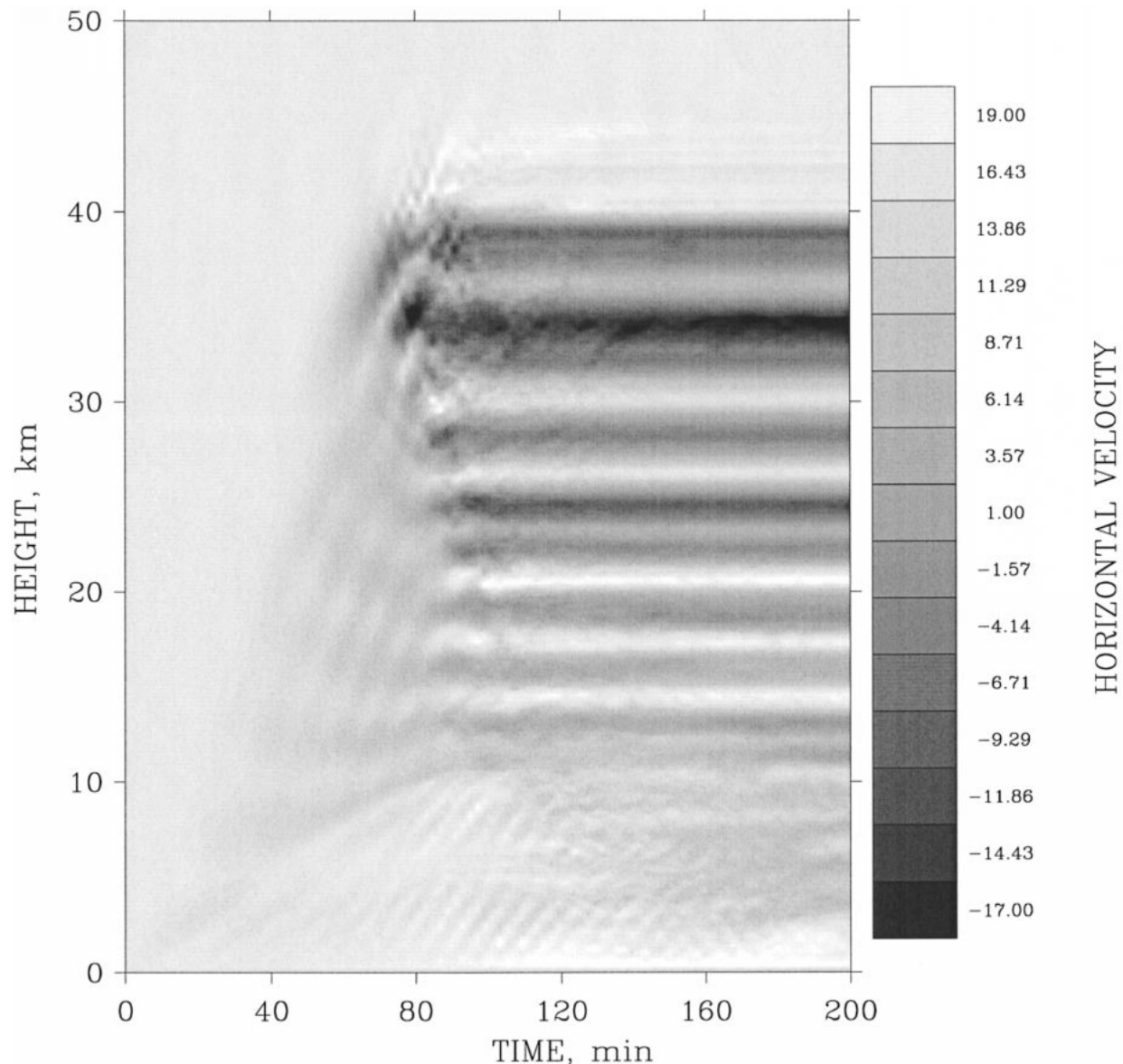


FIG. 6. Hovmöller plots of horizontal velocity (u_x) averaged at different horizontal levels for the simulation with $\phi = 56^\circ$ (expt 12 in Table 1).

dimensional internal waves, the three-dimensionalization of such breaking wave dominated flow, and finally upon the wave-mean flow interaction process itself.

a. Two-dimensional instability

A series of two-dimensional simulations has been performed for different values of the nondimensional parameter F_h (Table 1). Accordingly, the angle (ϕ) between the vertical and the wave crests has been varied in the range $\phi = 10^\circ$ – 70° . In all of our numerical experiments the upward propagation and subsequent breaking of gravity waves were observed. Although the breaking process was qualitatively different for

waves characterized by different values of the angle ϕ , some typical common features of the process could be isolated in all cases. The standard scenario for flow development is the following. First, the wavefront propagates upward, leaving in its wake an initially steady wave field. The wave field established behind the advancing front thereafter becomes unstable upon the development of typical S-shaped structures in the streamfunction. These S-shaped structures may achieve significantly supercritical amplitude before they finally break due to the onset of intense convective instability, consistent with the stability analysis by Winters and Riley (1992). In addition to this, the propagating wave front itself becomes unstable though the

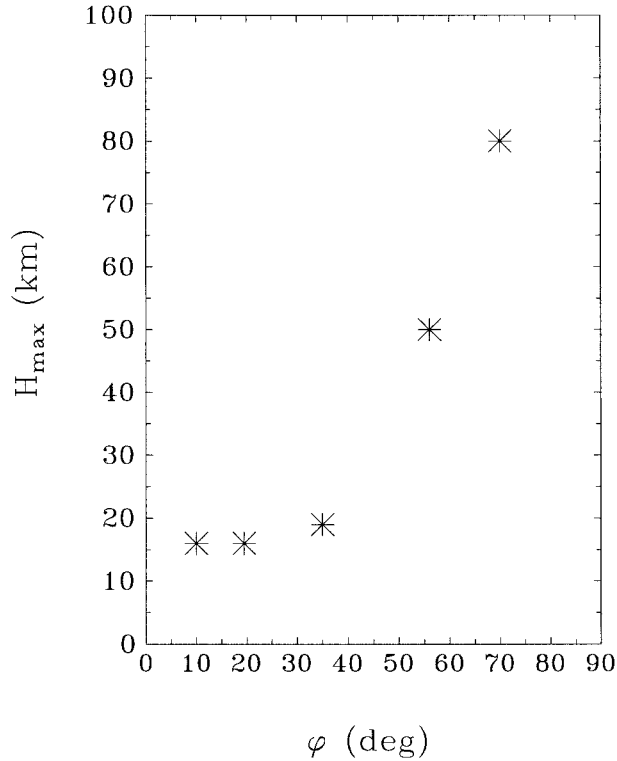


FIG. 7. Altitude of the wave front breaking region for different values of the angle ϕ .

appearance of an instability differs significantly from that of the established wave. Some S-shaped structures also develop at the front but these exhibit both counterclockwise and clockwise rotation (e.g., see the S-shaped feature indicated by an arrow in Fig. 5b). The feature shown in Fig. 5b is most probably induced by strong shear at the front itself, which results in the observed clockwise overturning (see Figs. 2d and 5b) in contrast to the case of the steady wave field behind the advancing front, where the overturning exhibits only a counterclockwise sense of rotation. Wave front breaking is usually more intense than the breaking of the established wave in terms of the amplitudes of the perturbations that developed thereafter. The instability of the wave front is most probably a consequence of steepening of the wave front (increasing vertical gradients) due to nonlinear effects. Note that this form of instability necessarily develops when the wave front reaches the sponge layer at the top of the computational domain. In this case, breaking occurs at the lower boundary of the sponge. Since the sponge smooths all perturbations to the background state by design, it artificially sharpens the wave front, thus inducing the instability.

The altitude of such wave front breaking strongly depends on the degree of hydrostaticity of the wave. In the case of a nonhydrostatic wave that propagates almost

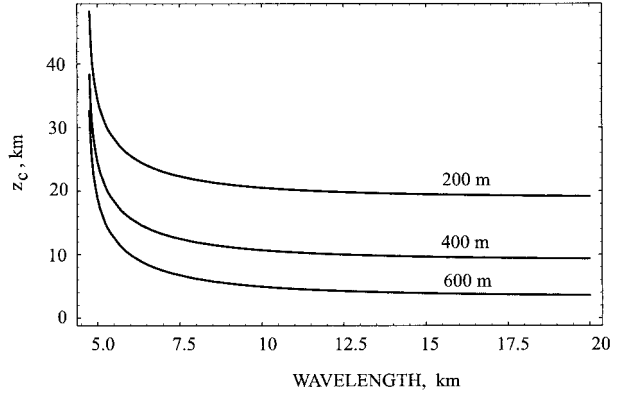


FIG. 8. Altitude of the critical steepening level (20) as a function of wavelength (km) for the wave of different amplitudes $h = 200, 400, 600$ m.

vertically (expts 1–5 in Table 1), overturning and breaking of the wave occurs at relatively low altitude (12–14 km when $\phi = 19.5^\circ$, see Figs. 2, 3). The breaking wave transfers significant momentum to the mean flow, causing significant deceleration. A narrow jet with negative velocity forms as a result of this interaction. The jet can be clearly seen in contour plots of horizontal velocity in Fig. 3. This jet is of course associated with a double critical layer with positive and negative values of vertical shear on its upper and lower flanks. This critical layer significantly inhibits further upward propagation of the wave so that only very weak wave activity is observed in the overlying region. Note, however, that weak, wavelike perturbations are transmitted that thereafter propagate upward and finally break at higher altitude. This secondary breaking occurs, for example, near an altitude of 60 km when $\phi = 19.5^\circ$ (see, e.g., Fig. 4, about 10 vertical wavelengths higher than the primary breaking level at 15 km). Since the amplitude of perturbations increases with altitude as e^{2H} , one can estimate the ratio of amplitudes of the primary wave and the secondary perturbation transmitted through a critical level, as $e^{\Delta z_c/2H}$, where Δz_c is the difference between the altitudes of breaking of these waves. For the case shown in Fig. 4 the difference is 40 km, which gives a ratio of amplitudes equal to approximately 17. In terms of “wave activity” (see, e.g., Scinocca and Peltier 1994), which is to leading order quadratic in the disturbance amplitude, the secondary disturbance is 300 times weaker than the primary wave. Such a weak transmission of waves through the critical layer is most probably due to the fact that this layer can be itself subject to wavelike motion as a whole and is not completely homogeneous along its length.

Considering the simulations in the sequence from small to larger angles it will be observed (e.g., $\phi = 71^\circ$, Fig. 5) that the primary breaking of the wave front occurs at successively higher elevations. As the wave becomes more strongly hydrostatic, its front breaks at

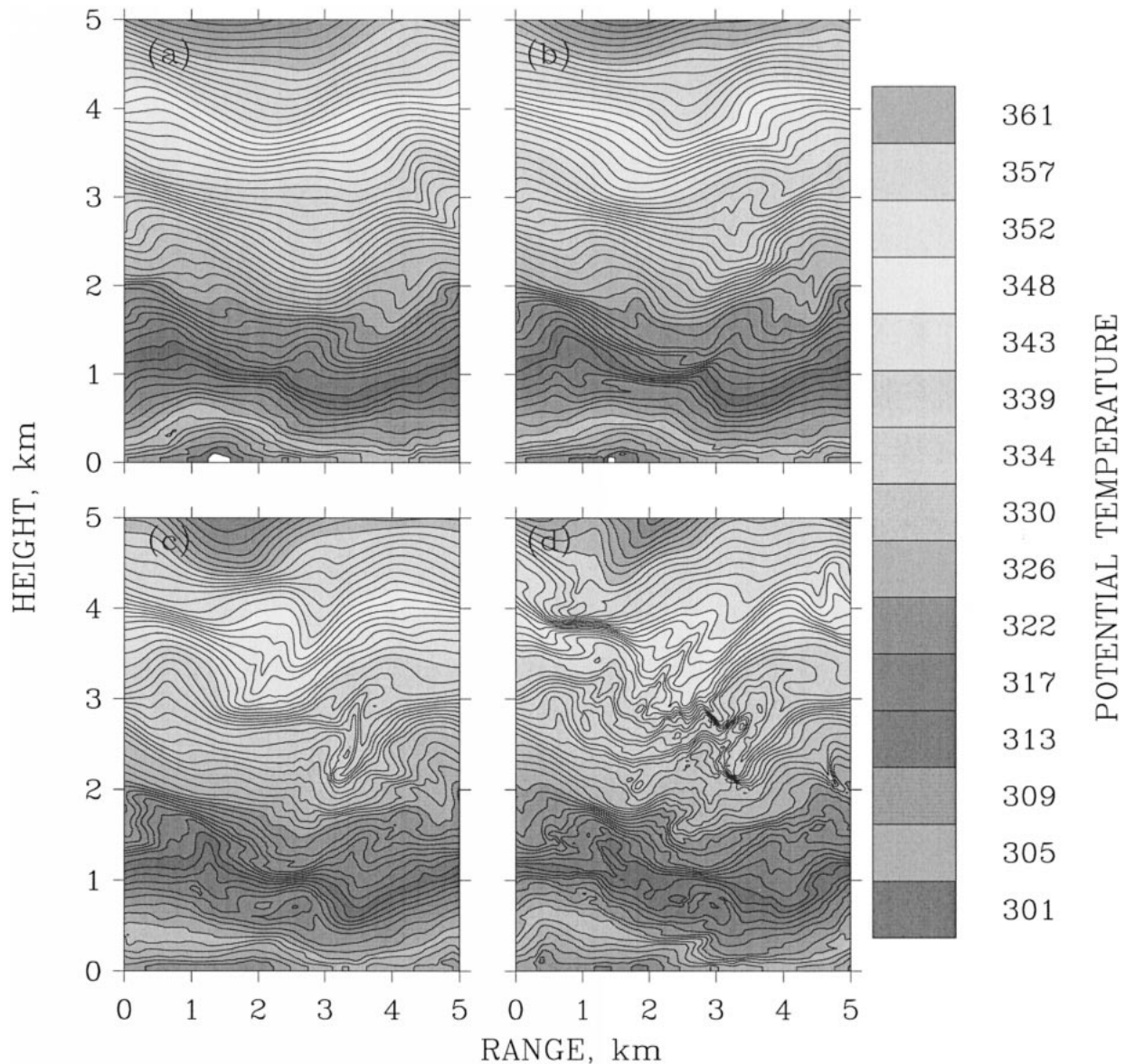


FIG. 9. Contour plots of potential temperature for the simulation with $\phi = 19.5^\circ$ (expt 5 in Table 1), (a) $t = 42.5$, (b) 50, (c) 57.5, (d) 65 min.

higher elevation and several distinct negative velocity jets (critical layers) thereafter form at different altitudes (Fig. 6) due to the breaking of the wave established below the front. Thus the region over which breaking occurs for hydrostatic waves is much deeper than that for nonhydrostatic waves, and the altitude of the upper boundary of this region, which is determined by wave front breaking, increases with the angle ϕ (Fig. 7).

One can easily estimate the height of the critical steepening level at which the wave is supposed to break according to the saturation theory. The condition for instability of the wave is $\partial\zeta/\partial z > 1$ where $\zeta(x, z)$ is the free stream deflection (see Peltier and Clark 1979). For

a steady linear wave $\zeta(x, z)$ has the following functional form:

$$\zeta(x, z) = h \exp\left(\frac{z}{2H}\right) \cos\left[kx + \left(\frac{N^2}{U^2} - k^2 + \frac{1}{4H^2}\right)^{1/2} z\right].$$

In the limit of large H , a solution of

$$\frac{\partial\zeta}{\partial z}(x, z) - 1 = 0$$

takes the form

$$z_c = -2H \ln\left[kh\left(\frac{N^2}{U^2 k^2} - 1\right)^{1/2}\right]. \quad (20)$$

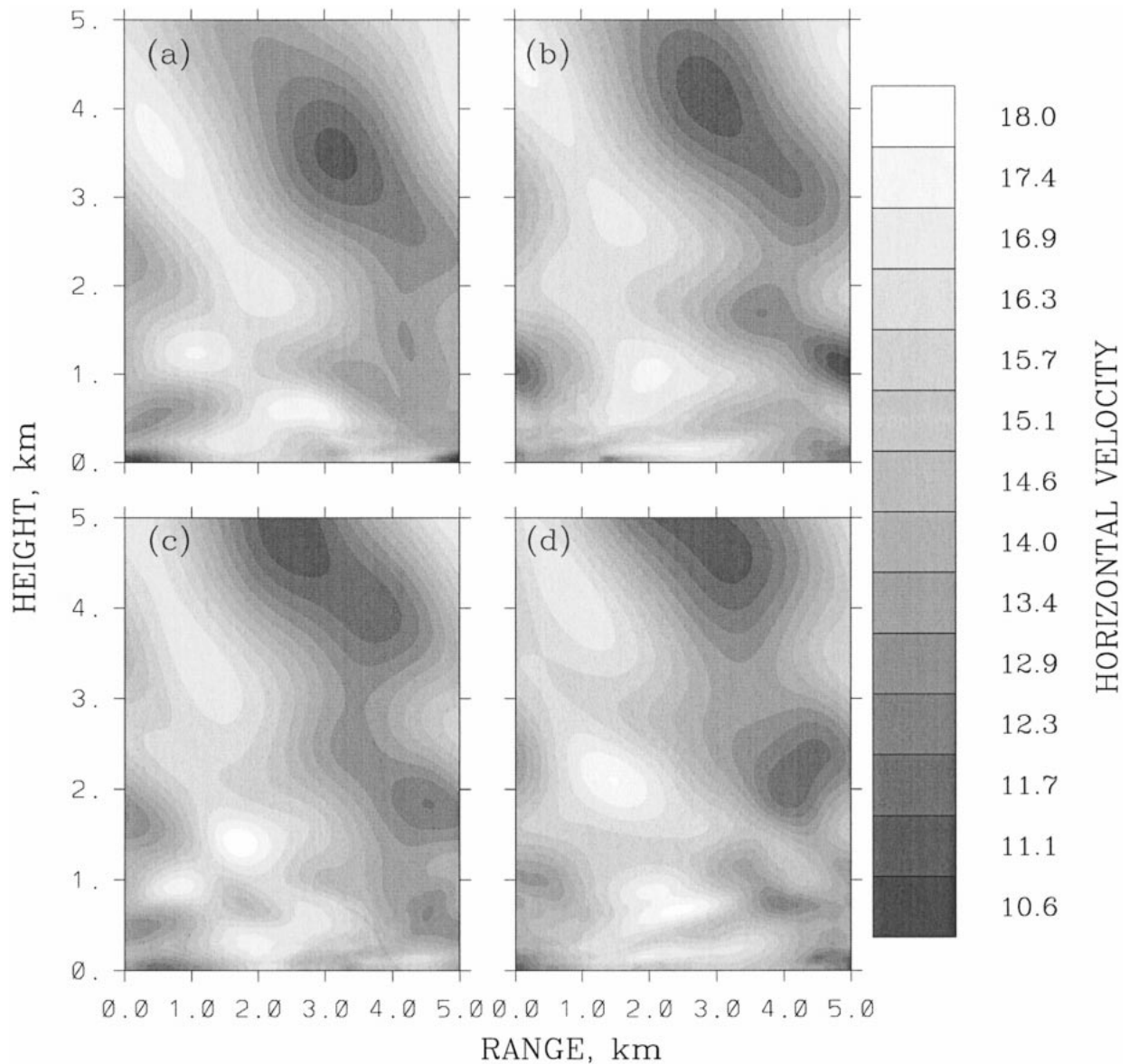


FIG. 10. As in Fig. 9 but for horizontal velocity (u_x) at (a) $t = 15$, (b) 17.5, (c) 20, (d) 22.5 min.

The graph of z_c as a function of horizontal wave length when the amplitude of the topography is 200 m as shown in Fig. 8. It is interesting to note that, in all our simulations, the lower boundary of the breaking region is

found to be significantly lower than that given by the estimate (20). For hydrostatic waves the lowest breaking altitude is determined by the breaking of regular waves established below the front (which breaks at high alti-

TABLE 2. Parameters used in three-dimensional numerical experiments.

Experiment	Δx (m)	N_x	Δz (m)	N_z	Δy (m)	N_y	a (km)	h (m)	ϕ ($^\circ$)	K_M ($m^2 s^{-1}$)
1	25	200	100	300	100	50	5	200	19.5	
2	25	200	100	300	25	50	5	200	19.5	
3	25	200	50	450	25	50	5	200	19.5	
4	25	200	70	300	50	50	5	200	19.5	0.5
5	25	200	70	300	50	50	5	200	19.5	50
6	42	200	200	250	50	50	8.4	200	56	
7	42	200	200	250	50	50	8.4	200	56	50

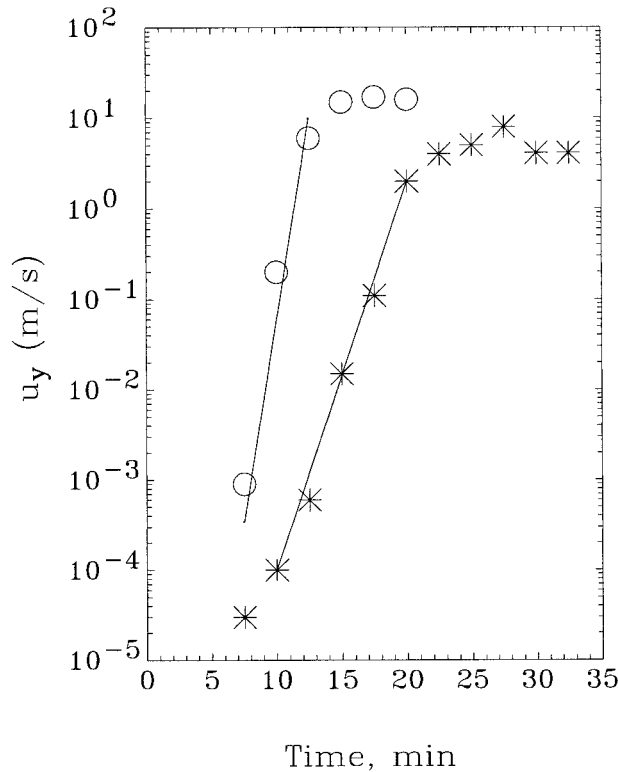


FIG. 11. Maximum values of cross-stream velocity (u_y) vs time of three-dimensional simulation for two experiments: (○) expt 6, (*) expt 7 (Table 2). Solid lines indicate the period of exponential growth.

tude), while for nonhydrostatic waves the lowest breaking altitude is determined by breaking at the wave front itself.

Another interesting phenomenon that we have observed in our simulations concerns the instability of small-amplitude waves that develops at the lower boundary. Typical results for flow evolution at low levels ($z = 0-5$ km) from a two-dimensional simulation (expt 5, Table 1) is shown in Figs. 9 and 10. The series of contour plots of potential temperature (Fig. 9) demonstrate the development of instability that is clearly identifiable as a parametric subharmonic instability

(PSI) (see, e.g., Klostermeyer 1991; Thorpe 1984b) both on the basis of the fact that it originates in subharmonic waves (Fig. 9a) of frequency ω_1 , which is half the frequency ω of the primary wave as well as its finite-amplitude form (localized overturning motions) (Figs. 9c,d). One can easily show that the observed instability is indeed PSI by estimating the angle at which the subharmonic waves are inclined. Since the primary wave is at an angle ϕ to the vertical, and frequency can be related to the angle via a simplified dispersion relation

$$\omega = N \cos \phi,$$

one can obtain the angle ϕ_1 for the subharmonic waves in the form

$$\phi_1 = \arccos\left(\frac{1}{2} \cos \phi\right)$$

using the dispersion relation of the same form and assuming $\omega_1 = \omega/2$. In our particular case $\phi = 19.5^\circ$, hence $\phi_1 = 61.9^\circ$ (subharmonic waves are more horizontal, as one would expect). Direct measurement of the angle ϕ_1 from the horizontal velocity field shown in Fig. 10 gives the value $\phi_1 = 62.5^\circ \pm 1^\circ$, which is in very good agreement with the theoretical result. PSI is initiated from the very beginning of the simulations and evolves to its finite-amplitude form during about 10 buoyancy periods. Our simulations show that the growth rate of this instability depends on the hydrostaticity parameter as well as on nonlinearity parameters. For waves with the same amplitude (200 m) the instability develops relatively quickly and assumes its most intense finite-amplitude form when the waves are nonhydrostatic. For the angles $\phi > 50^\circ$ the instability becomes dynamically insignificant. However, the series of simulations (expts 7, 8, 9 in Table 1) of the waves with the same angle $\phi = 49^\circ$ but with different amplitude ($h = 200, 400, 600$ m) shows that while negligible at smaller amplitude, the instability develops for larger-amplitude ($h = 400, 600$ m) waves and becomes more intense with larger amplitude. Note that this instability does not totally destroy the coherence of the primary wave field, however, probably because of the highly

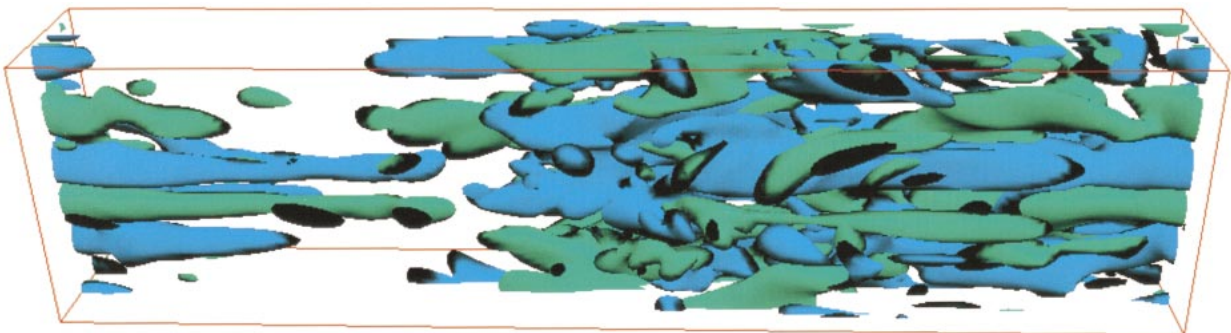


FIG. 12. Isosurfaces of the streamwise component of vorticity: $\omega_x = \pm 2 \times 10^{-3} \text{ s}^{-1}$ (expt 7 in Table 2), $t = 97.5$ min (27.5 min of three-dimensional simulation initialized from two-dimensional initial conditions).

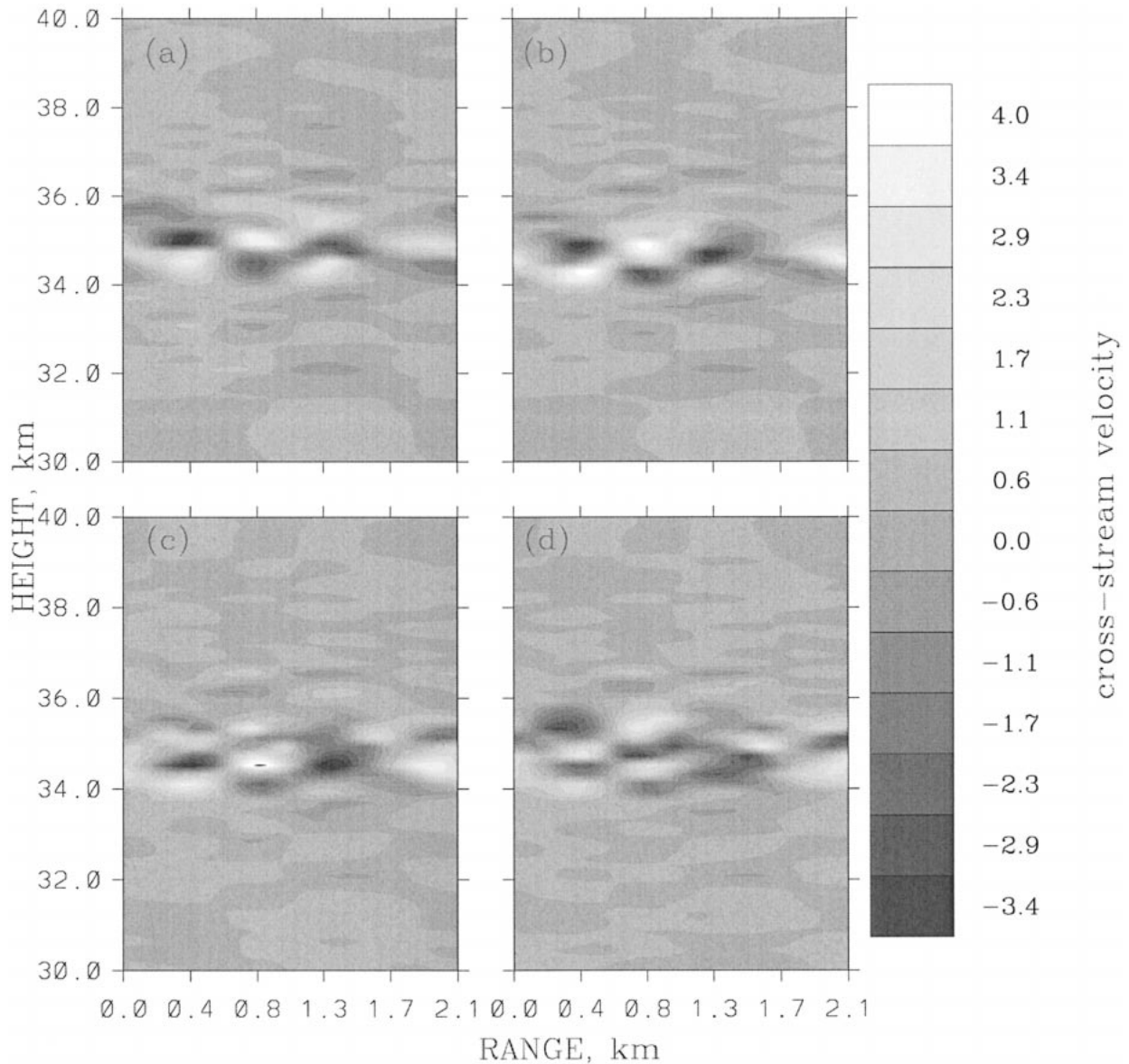


FIG. 13. Contour plots of cross-stream component of velocity (u_y) at different y - z planes: (a) $x = 0.63$, (b) 0.84 , (c) 1.05 , (d) 1.26 km (expt 7 in Table 2), $t = 100$ min.

localized spatial structure of the subharmonic disturbances. As a consequence, the onset of PSI does not prevent breaking of the primary wave at higher altitude at later times.

b. Three-dimensional instability

To study the modification of the above-described two-dimensional flows when the flow is allowed to access the third spatial degree of freedom, we employ two-dimensional experiments 3, 4, 5 ($\phi = 19.5^\circ$) and experiment 11 ($\phi = 56^\circ$) (Table 1) in order to initialize the evolution of the three-dimensional flows (expts 1–7,

Table 2). The flow was first allowed to develop in three dimensions only after some time of two-dimensional integration, a time by which wave breaking had yet to commence. Prior to overturning, our three-dimensional results duplicate two-dimensional results to high accuracy because spanwise instabilities show negligible growth. The growth of spanwise instability onsets as the waves begin to overturn. The characteristics of the instability thereafter reveal dependence on the degree of nonhydrostaticity as with other characteristics of the flow as described above. The first three-dimensional run (expt 1, Table 2) for the nonhydrostatic wave shows that three-dimensional motions do occur and evolve in the

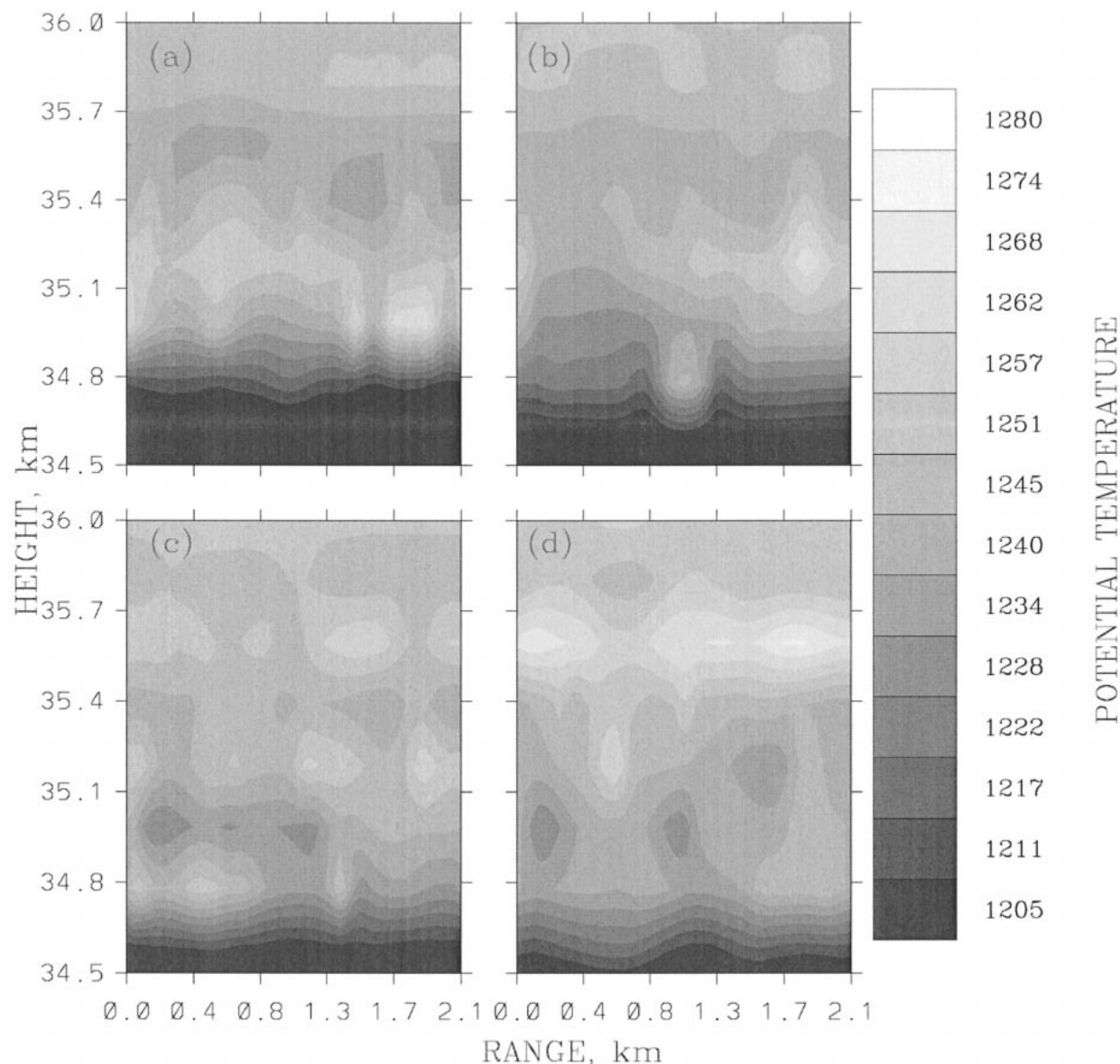


FIG. 14. Contour plots of potential temperature at different y - z planes: (a) $x = 5.25$, (b) 5.46 , (c) 5.67 , (d) 5.89 km (expt 7 in Table 2), $t = 97.5$ min.

flow. The perturbations appear in the wave breaking region and their initial growth is close to exponential. After approximately 15 min of three-dimensional simulation, the amplitude of fluctuations of cross-stream velocity, which is an indicator of three-dimensional motions, becomes comparable with the velocity (U) of the background wind. The typical spanwise scale of these perturbations was, however, almost the same as the scale (Δy) of our computational grid in the y direction. Since the clear identification of the spanwise scale of the perturbation is obviously a problem of numerical resolution, we performed two additional simulations with increased spanwise and vertical resolution (expts 2, 3,

Table 2). However, the scale of the perturbation always remained the same as the grid scale for all values of $\Delta y = 25$ – 100 m. Thus, we were unable to isolate the actual physical scale of the perturbations in the cross-stream direction. Since these perturbations are, most probably, of convective type (similar to the previously described K–P instability), the analogy with Rayleigh–Taylor instability suggests that the growth rate of the instability monotonically increases with decreasing wavelength in the absence of dissipative processes (viscosity and diffusivity). Thus it is expected to be impossible to numerically resolve the fastest growing shortest wavelengths when viscosity is very small. Note that in sim-

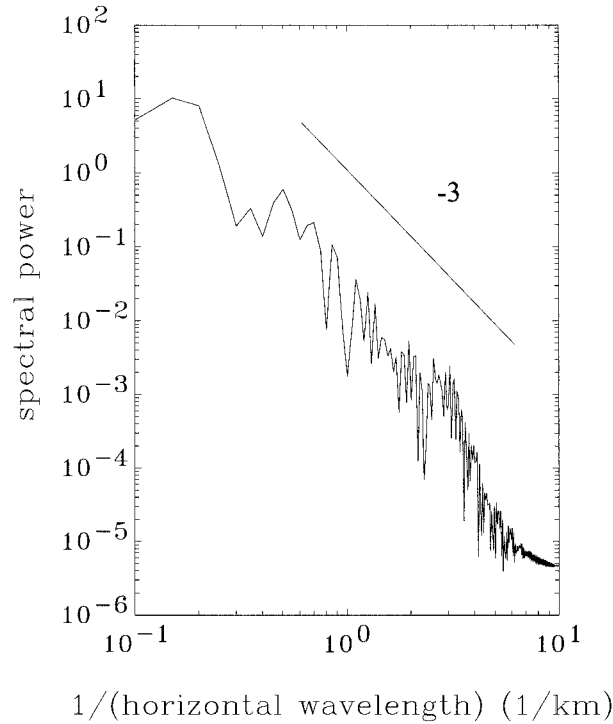


FIG. 15. Spectrum of cross-stream velocity (u_x) at altitude 33 km (expt 17 in Table 1), $t = 102.5$ min.

ulations 1–3 the nonuniform distribution of viscosity (11) with coefficient $c = 0.23$ was employed. It is useful to define the Rayleigh number of the flow as

$$\text{Ra} = \frac{h^4 N^2}{K_M K_H},$$

where h is the amplitude of the overturning wave. Using (11) and scaling deformation as $\text{def} \propto U/h$ one may approximate the Rayleigh number as

$$\text{Ra} = \frac{h^6 N^2}{c^4 (\Delta x \Delta z)^4 U^2} \quad (21)$$

in the regions of the flow where $\text{Ri} < 1$. For typical values of the parameters in (21) the Rayleigh number is extremely large, with values in the range 10^8 – 10^9 . These large values of the Rayleigh number imply that the instability is expected to evolve vigorously and to have an unresolvably small initial wavelength that is consistent with the results of our simulations. To study the evolution of the instability in the flow with different values of the diffusivity parameters, we employed a uniform value of viscosity $K_M = 0.5 \text{ m}^2 \text{ s}^{-1}$ in experiment 4 and $K_M = 50 \text{ m}^2 \text{ s}^{-1}$ in experiment 5. We may define the Reynolds number of the flow as

$$\text{Re} = \frac{U(U/N)}{K_M}.$$

The values of the Reynolds number for experiments 4 and 5 are 4.5×10^4 and 450, which can be characterized

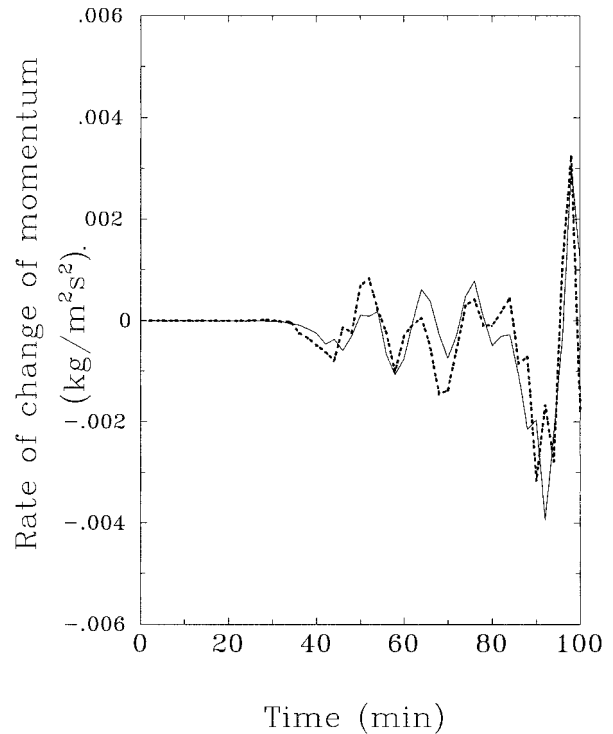


FIG. 16. Rate of change of momentum for different times in the horizontal layer at altitude of 22 km for the simulation 12 (Table 1). Solid and dotted curves represent left and right sides of (22), respectively.

as high and moderate, respectively. The corresponding value of the Rayleigh number for experiment 4 is still very high ($\text{Ra} \approx 10^9$) while for experiment 5 it is four orders of magnitude less ($\text{Ra} \approx 10^5$). Experiment 4 gave similar results as those obtained in the previous experiments as one might expect. In experiment 5 the instability was characterized by negligible growth, it being strongly suppressed by viscous diffusion. Thus, in the case of the nonhydrostatic wave, our results are inconclusive concerning the spanwise scale of the three-dimensional instability that develops as the wave breaks.

It turned out, however, that it was possible to obtain some insight into spanwise structure of the instability in the simulations of the waves characterized by higher degrees of hydrostaticity ($\phi = 56^\circ$). Experiment 6 (Table 2) with large Rayleigh number (nonuniform K_M , $c = 0.23$) gave a result similar to that obtained for nonhydrostatic waves, namely, the amplitude of three-dimensional instability grows exponentially (Fig. 11) during the first 10 min of three-dimensional simulation until it saturated at the level of background velocity U , while the spanwise scale of the instability remained unresolved. However, experiment 7 with a smaller value of the Rayleigh number revealed well-resolved spanwise structure of the instability, though in this case the growth rate of the instability was lower (Fig. 11). The instability grows approximately exponentially, $u_x \propto e^{\gamma t}$, during the

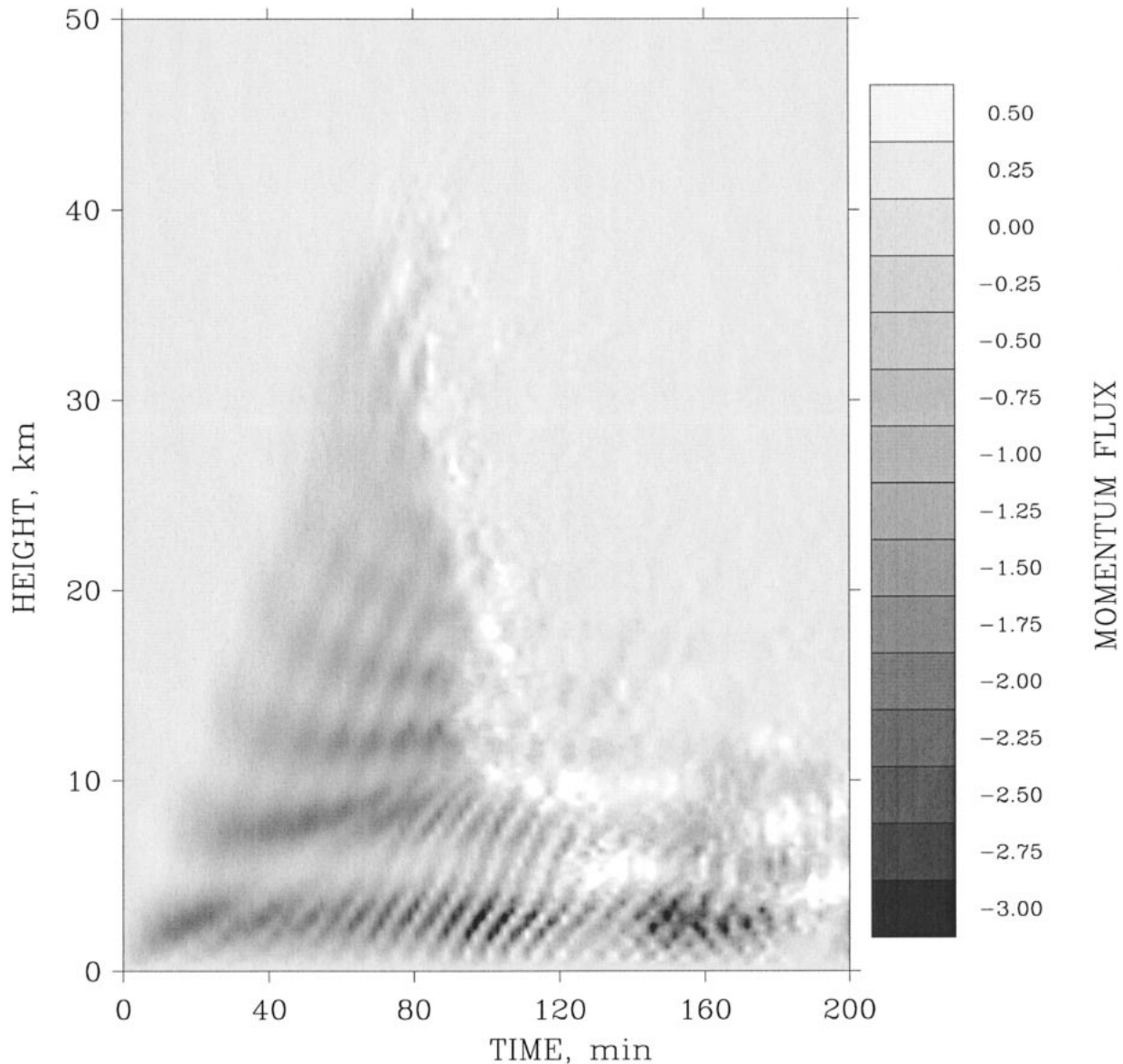


FIG. 17. Hovmöller plot of vertical flux of the horizontal momentum ($\overline{\rho u'w'}$) averaged at different horizontal levels for the simulation with $\phi = 56^\circ$ (expt 12 in Table 1).

first 5–15 min (1–3 buoyancy periods $T = 2\pi/N \approx 5$ min) after which the instability saturates. The growth rates for the instability estimated from the data shown in Fig. 11 are $\gamma = 0.014, 0.029 \text{ s}^{-1}$ (in nondimensional form $\gamma/N = 0.68, 1.5$) for $Ra = 10^5, 10^9$ respectively.

These values can be compared with the results of stability analysis (Thorpe 1984a) for static instability of a viscous and diffusive flow with the density profile

$$\rho_1 = \rho_0 \left[1 - \frac{N^2}{g}z + A \sin(Kz) \right],$$

which can be taken to represent (locally) the overturning gravity wave. Thorpe's analysis shows that growth rates

depend on Rayleigh and Prandtl numbers as well as on a parameter, $r = N^2/gKA$, that describes the shape of the density profile. When $r < 1$ the density profile considered is locally unstable ($d\rho_1/dz < 0$) to overturning convective instability. In his Fig. 6 Thorpe presents growth rate for different values of r as functions of Ra . Thorpe's results were extended by Sonmor and Klaassen (1997) to higher Rayleigh numbers (the largest value considered by Thorpe was $Ra = 10^5$) and presented in their Fig. 17. Since in our case the wave breaks at an altitude of approximately 36 km, its amplitude is approximately 10 times that of its minimal breaking amplitude [which is achieved at the height z_c (20)]. Thus, the growth rates of convective instability obtained in

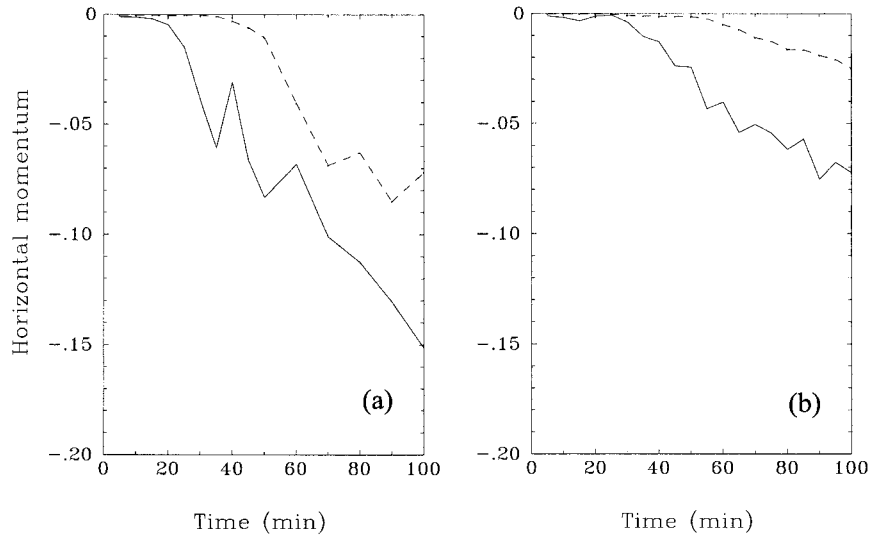


FIG. 18. The difference between the momentum (per unit length) horizontally averaged at different altitudes and the momentum of the background wind, $\bar{p}(z)U$, normalized by the value of the background momentum, $\rho_0 U$ at the ground, as the function of time, for two simulations: (a) expt 7 (Table 1), altitude 10.4 km (solid line), 18 km (streak line); (b) expt 14, altitude 10 km (solid line), 22 km (streak line).

our simulations might be compared with those delivered by linear stability analysis for the value of inverse amplitude $r = 0.1$ and the values of Rayleigh number $Ra = 10^5, 10^9$. Though direct comparison is not possible since the values of the growth rate for $r = 0.1$ are not provided in Sonmor and Klaassen (1997) (the value of the Prandtl number is also different), our values are still in qualitative agreement with the values given in their Figs. 17 and 19. The three-dimensional perturbations have the typical form of an array of streamwise vortex tubes of alternating sign (Figs. 12, 13). The instability is highly localized in the region of wave breaking between 34 and 36 km and is very intense. In Fig. 14 one will observe significant perturbations of the (initially uniform in the spanwise direction) potential temperature field caused by the instability. Since there are typically three vortex pairs in the spanwise direction within the model domain, the dominant spanwise wavelength λ_y of the perturbation is estimated to be $\lambda_y \approx 0.7$ km or $\lambda_y N/U \approx 1$ in nondimensional units. The growth of three-dimensional perturbations finally leads to development of fully three-dimensional turbulence with a spectrum (Fig. 15) with a “-3” slope that is typical for the spectra of internal gravity waves (see, e.g., Smith et al. 1987). Note, however, that the mean flow remains essentially two-dimensional.

c. Wave-mean flow interaction

Gravity waves force the mean flow through the Reynolds stress associated with the divergence of the vertical flux of horizontal momentum of the waves. The balance of horizontal momentum is given by the well-known Reynolds averaged relation

$$\rho \frac{\partial U}{\partial t} = \frac{\partial}{\partial z} (\overline{\rho u' w'}), \quad (22)$$

where u' , w' are the fluctuations of the horizontal and vertical components of velocity. A typical example of the time evolution of the instantaneous horizontally averaged rate of change of momentum [left-hand side of (22)] at some altitude is shown in Fig. 16 in comparison with the Reynolds stress divergence [right-hand side of (22)]. The agreement is entirely satisfactory within the accuracy of the averaging procedure and finite-difference numerical evaluation of derivatives. The divergence of momentum flux causes deceleration and acceleration of the mean flow in layers at different altitudes (e.g., Fig. 6). While the effect of acceleration is not particularly strong, the velocity in decelerated regions reaches very high negative values. Note that under the assumption that linear waves propagate into pre-existing undisturbed mean flow, the waves would be unable to drive the mean wind beyond the initial phase speed of the waves (in our case the initial wave is stationary, hence $c = 0$). The process of adjustment in the phase speed of the wave motion in a region of decelerated mean wind is an essentially nonlinear process and has been called self-acceleration (see, e.g., Fritts and Dunkerton 1984). An important influence on the wave-mean flow interaction is also wave transience. During the propagation of the wave front, wave transience forces the mean flow, causing transient buildup of the mean wind. As has been noted previously by Walterscheid and Schubert (1990), and supported by the present simulations, the major part of the mean wind buildup is a consequence of wave transience. It is clear that wave transience has an important influence in the

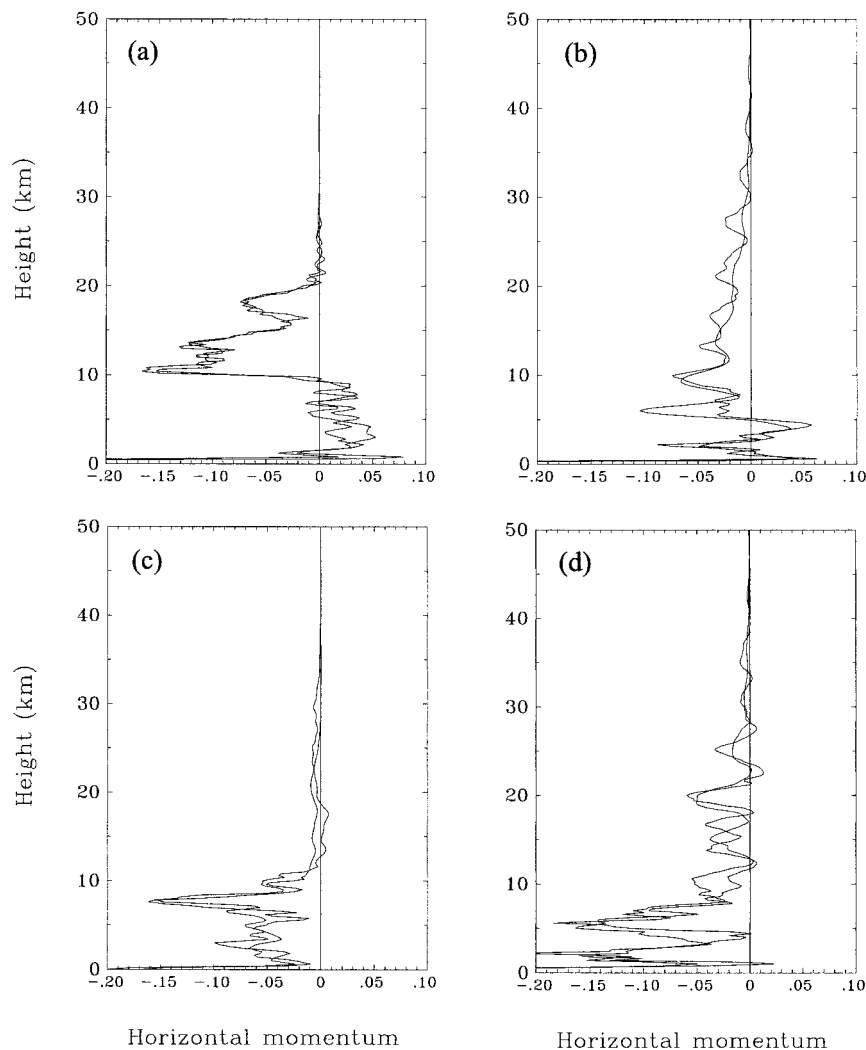


FIG. 19. Normalized horizontal momentum (as in Fig. 18) as the function of height, z (km) for four simulations: (a) expt 7 (Table 1), (b) expt 14, (c) expt 15, (d) expt 16. Solid lines represent momentum profiles at $t = 80, 100$ min.

overall process of wave-mean flow momentum transfer. Ultimately, breaking of the nonlinear transient waves leads to dramatic irreversible changes in the mean flow. Figure 17 shows a Hovmöller diagram for momentum flux averaged in the horizontal for every instant of time. The altitude-time dependence of the momentum flux is consistent with that of the horizontal velocity shown in Fig. 6. The intense initial breaking of the wave in a deep region between the altitudes of 10 and 40 km at about 80 min generates a structure of alternating decelerated and accelerated layers. The transfer of momentum at low levels is most probably a consequence of reflections and/or backscattering of the upward-propagating waves from the turbulent breaking region. The reflected downward propagating waves in the lower layer can be seen in the momentum flux diagram of Fig. 17 after about 130 min of simulated time. Note that, in the layers where the deposition of momentum takes place, the velocity

(hence horizontal momentum) changes at an approximately constant rate after the onset of wave breaking, indicating a constant rate of momentum deposition at these levels. Figure 18 illustrates the typical time dependence of the horizontal momentum for two simulations ($\phi = 49^\circ, 71^\circ$). The difference between the momentum (per unit length) horizontally averaged at two different altitudes and the momentum of the background wind, $\bar{\rho}(z)U$, normalized by the value of the background momentum, $\rho_0 U$ at the ground, is shown. Two levels at which the momentum transfer achieves its maximum values were chosen.

The dynamics of momentum transfer illustrates the dependence on the degree of hydrostaticity of the waves, as might be expected on the basis of the different characteristics of the breaking process for different values of the angle ϕ . Figures 19a,b show typical vertical profiles of the normalized horizontal momentum for two

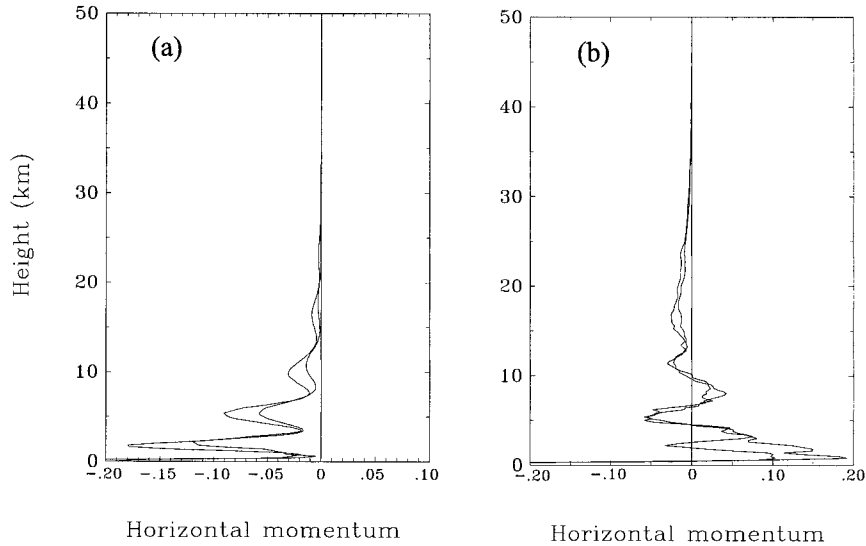


FIG. 20. Normalized horizontal momentum (as in Fig. 18) as the function of height, z (km) for two simulations: (a) expt 17 (Table 1), (b) expt 18. Solid lines represent momentum profiles at $t = 100, 125$ min.

simulations ($\phi = 49^\circ, 71^\circ$). Inspection of these results clearly demonstrates that the region in which the wave transfers negative momentum to the mean flow is localized in the narrow layer between 10 and 20 km when $\phi = 49^\circ$ but extends to 40 km for the more hydrostatic wave with $\phi = 71^\circ$.

An important question, clearly, concerns the way in which the results for monochromatic waves will change when several interacting waves of different wavelengths (which may also be of different amplitude) are present in the domain. This question obviously deserves separate detailed study; however, we have made a preliminary attempt to approach this problem here. Two simulations (expts 15, 16 in Table 1) were performed with a spectrum consisting of three waves. The waves with the angles ($\phi = 7^\circ, 49^\circ, 71^\circ$) represented nonhydrostatic, intermediate, and hydrostatic parts of the spectrum. In the first simulation the amplitudes of the waves were assumed to be equal to each other (a white spectrum) and 200 m in total amplitude to enable comparison with the monochromatic simulations. In the second simulation the amplitudes were varied with wavelength (red spectrum), the longest wave having the largest amplitude. This (red) form of the spectrum should be more relevant to understanding the breaking of a spectrum of waves generated by real topography for which the typical vertical scales are proportional to horizontal scales in first approximation. The horizontal momentum profiles for these two simulations are shown in Figs. 19c,d for the same moments of time as the profiles for monochromatic waves (Figs. 19a,b). Comparing Figs. 19d and 19b it is clear that spatial structure, that is, the altitudes of peaks of negative momentum and the total vertical extent of the momentum transfer region, are very similar in both cases, which allows us to suggest that the longest

(hydrostatic) wave having the largest amplitude dominates in determining the spatial structure of the controlling critical layers. Shorter waves are effectively absorbed by these layers (especially at the low levels). Since the total amplitude of the waves is two times larger than the amplitude of the monochromatic wave, the peaks are larger, which demonstrates that shorter waves also contribute to the momentum transfer process. In the simulation in which all waves were assumed to have the same amplitude, the nonhydrostatic part of the spectrum was found to dominate and this resulted in a narrow region of momentum transfer confined to a lower level (Fig. 19c).

To consider a limiting case of wave–wave interaction that forms the basis of Hines’s (1997) parameterization scheme we return now to an even simpler configuration consisting of a very long wave and a short wave, a configuration where Hines’s mechanism is expected to work well. Two simulations (expts 17 and 18 in Table 1) were performed with the waves ($\phi = 10^\circ, 84^\circ$) that differ by a factor of 9 in wavelength and of different amplitudes. In the first simulation the amplitude of the short wave is 9 times less than the amplitude of the long wave, while in the second simulation it is only 2 times less. It is clear in both simulations that breaking of the short wave is spatially localized at maxima of the long wave at lower altitudes, while at higher altitudes, where the short wave acquires an amplitude large enough to break on its own without the “help” of the wind due to the long wave, the breaking is more spatially uniform. This behavior is consistent with Hines’s theory. The horizontal momentum profiles (Fig. 20) for these two simulations are qualitatively similar to the three-wave profiles in Figs. 19c and 19d, respectively, which once

more indicates the relative domination of shorter or longer waves in these two cases.

4. Discussion

The numerical simulations described herein provide clear evidence that the dynamics of internal gravity wave breaking strongly depends on the degree of hydrostaticity (represented by the nondimensional parameter F_h) of the wave. In general, the transfer of momentum from the breaking wave to the mean flow takes place inhomogeneously in space and results in the formation of one or more horizontal jets of low (or negative) velocity at different altitudes. The breaking of the wave field occurs due to two main effects, respectively involving the instability of the wave front itself and the instability of the wave established behind the advancing front. The altitude at which the wave front breaks increases with increasing hydrostaticity of the wave, thus leading to a deeper region in which the waves effectively transfer momentum to the mean flow.

Our three-dimensional simulations initialized from two-dimensional initial conditions demonstrate that such an overturning primary wave becomes convectively unstable to a higher-order instability. This higher-order instability is a shear-aligned instability of convective type that first appears in the form of streamwise-oriented vortices of alternating sign. The spanwise lengthscale of the perturbations turns out to be very sensitive to the degree of diffusion of momentum and heat, which can be expressed in an appropriate Rayleigh number (the value of the Prandtl number $Pr = 1$ was fixed in our numerical experiments).

It is useful to consider the results of our simulations in comparison with the two main gravity wave drag parameterization schemes mentioned in the introduction. Although our simulations show that a monochromatic wave propagating through a region of uniform wind will break due to its intrinsic degree of instability, as one would expect in the context of saturation theory based on the hypothesis that a wave necessarily breaks when its amplitude is supercritically steepened, the character of the instability and the spatial distribution of the breaking region are highly variable in our simulations. Our results demonstrate both that the lowest breaking level is always lower than the critical steepening level and that breaking of the unsteady wave front is a dynamically important process. Neither the instability of the front nor the instability of the wave established in the region behind the advancing front can be characterized as simple gravitational convective instabilities but rather are most probably enhanced by shear with convective instability acting at later stages. Another feature of our results is the strong dependence of the spatial distribution of momentum transfer on the hydrostaticity of the wave. The region in which the waves deposit their momentum can be localized for nonhydrostatic waves or significantly diffused in the vertical for hy-

drostatic waves. Note that almost all of the momentum that enters the computational domain from the lowest boundary is transferred to the mean flow, only a small fraction (about 2%) escaping to the upper boundary of the domain where it is dissipated by Rayleigh friction in the "sponge." Thus it is hardly surprising that saturation theory gives the correct value of total momentum transferred to the mean flow by the waves generated at the lower boundary. This may be acceptable for general circulation models that at present have rather crude vertical resolution. However, our results suggest that the fine structure of the flow can be significantly different from that predicted by saturation theory, a fact that may be important for the next generation of large-scale circulation models.

Although an extensive study of the wave breaking process for a complete spectrum of waves is obviously needed (and is currently under way), our present simulations with three waves have allowed us to draw some preliminary conclusions. In accord with Hines's (1997) gravity wave drag parameterization theory based on critical layer absorption, we note that the waves are indeed absorbed at critical layers induced by other waves, representing different parts of the spectrum. However, in our simulations these critical layers are created as a result of wave breaking, permanently changing the mean flow, rather than being describable as critical layers that exist due to the presence of linear nonbreaking waves associated with the rest of the spectrum. This point would appear to be of fundamental importance and deserves further detailed investigation.

Acknowledgments. The research reported in this paper has been supported by the Natural Sciences and Engineering Research Council of Canada under Grant A9627.

REFERENCES

- Afanasyev, Ya. D., and W. R. Peltier, 1998: The three-dimensionalization of stratified flow over two-dimensional topography. *J. Atmos. Sci.*, **55**, 19–39.
- Andreassen, Ø., C. E. Wasberg, D. C. Fritts, and J. R. Isler, 1994: Gravity wave breaking in two and three dimensions. I. Model description and comparison of two-dimensional evolutions. *J. Geophys. Res.*, **99** (D), 8095–8108.
- , P. O. Hvidsten, D. C. Fritts, and S. Arendt, 1998: Vorticity dynamics in a breaking internal gravity wave. Part I. Initial instability evolution. *J. Fluid Mech.*, **367**, 27–46.
- Baines, P. G., 1995: *Topographic Effects in Stratified Flows*. Cambridge University Press, 482 pp.
- Caulfield, C. P., and W. R. Peltier, 1994: Three dimensionalization of the stratified mixing layer. *Phys. Fluids*, **6**, 3803–3805.
- Clark, T. L., 1977: A small-scale dynamic model using a terrain-following coordinate transformation. *J. Comput. Phys.*, **24**, 186–215.
- , and W. R. Peltier, 1977: On the evolution and stability of finite-amplitude mountain waves. *J. Atmos. Sci.*, **34**, 1715–1730.
- Dornbrack, A., 1998: Turbulent mixing by breaking gravity waves. *J. Fluid Mech.*, **375**, 113–141.
- Dunkerton, T. J., 1987: Effect of nonlinear instability on gravity wave momentum transport. *J. Atmos. Sci.*, **44**, 3188–3209.

- Durrán, D. R., 1986: Another look at downslope windstorms. Part I: The development of analogs to supercritical flow in an infinitely deep, continuously stratified fluid. *J. Atmos. Sci.*, **43**, 2527–2543.
- Fritts, D. C., and T. J. Dunkerton, 1984: A quasi-linear study of gravity-wave saturation and self-acceleration. *J. Atmos. Sci.*, **41**, 3272–3289.
- , and P. K. Rastogi, 1985: Convective and dynamic instabilities due to gravity wave motions in the lower and middle atmosphere: Theory and observations. *Radio Sci.*, **20**, 1247–1277.
- , J. F. Garten, and O. Andreassen, 1996: Wave breaking and transition to turbulence in stratified shear flows. *J. Atmos. Sci.*, **53**, 1057–1085.
- , S. Arendt, and O. Andreassen, 1998: Vorticity dynamics in a breaking internal gravity wave. Part 2. Vortex interactions and transition to turbulence. *J. Fluid Mech.*, **367**, 47–63.
- Gill, E. A., 1982: *Atmosphere–Ocean Dynamics*. Academic Press, 662 pp.
- Hamilton, K., 1999: The gravity wave parameterization problem for global simulation models. *SPARC Newslett.*, **12**, 7–14.
- Hines, C. O., 1971: Generalization of the Richardson criterion for the onset of atmospheric turbulence. *Quart. J. Roy. Meteor. Soc.*, **97**, 429–439.
- , 1997: Doppler-spread parameterisation of gravity wave momentum deposition in the middle atmosphere. Part 1: Basic formulation. *J. Atmos. Solar-Terr. Phys.*, **59**, 371–386.
- Holton, J. R., 1982: The role of gravity wave induced drag and diffusion in the momentum budget of the mesosphere. *J. Atmos. Sci.*, **39**, 791–799.
- Klaassen, G. P., and W. R. Peltier, 1985a: The onset of turbulence in finite-amplitude Kelvin–Helmholtz billows. *J. Fluid Mech.*, **155**, 1–35.
- , and —, 1985b: The effect of the Prandtl number on the evolution and stability of Kelvin–Helmholtz billows. *Geophys. Astrophys. Fluid Dyn.*, **32**, 23–60.
- , and —, 1985c: The evolution of finite amplitude Kelvin–Helmholtz billows in two spatial dimensions. *J. Atmos. Sci.*, **42**, 1321–1339.
- , and —, 1989: The role of transverse secondary instabilities in the evolution of free shear layers. *J. Fluid Mech.*, **202**, 367–402.
- , and —, 1991: The influence of stratification on secondary instability in free shear layers. *J. Fluid Mech.*, **227**, 71–106.
- Klostermeyer, J., 1991: Two- and three-dimensional parametric instabilities in finite amplitude internal gravity waves. *Geophys. Astrophys. Fluid Dyn.*, **61**, 1–25.
- Laprise, R., and W. R. Peltier, 1989a: The linear stability of nonlinear mountain waves: Implications for the understanding of severe downslope windstorms. *J. Atmos. Sci.*, **46**, 545–564.
- , and —, 1989b: On the structural characteristics of steady finite-amplitude mountain waves over bell-shaped topography. *J. Atmos. Sci.*, **46**, 586–595.
- Lilly, D. K., 1962: On the numerical simulation of buoyant convection. *Tellus*, **14**, 148–172.
- Lindzen, R. S., 1968: Lower atmospheric energy sources for the upper atmosphere. *Meteorological Investigations of the Upper Atmosphere, Meteor. Monogr.*, No. 9, Amer. Meteor. Soc., 37–46.
- , R. S., 1981: Turbulence and stress due to gravity wave and tidal breakdown. *J. Geophys. Res.*, **86**, 9707–9714.
- Lott, F., and H. Teitelbaum, 1993: Linear unsteady mountain waves. *Tellus*, **45A**, 201–220.
- McFarlane, N. A., 1987: The effect of orographically excited gravity wave drag on the general circulation of the lower stratosphere and troposphere. *J. Atmos. Sci.*, **44**, 1775–1800.
- McIntyre, M. E., 1972: On Long's hypothesis of no upstream influence in uniformly stratified or rotating flow. *J. Fluid Mech.*, **52**, 209–243.
- Peltier, W. R., and T. L. Clark, 1979: The evolution and stability of finite-amplitude mountain waves. Part II: Surface drag and severe downslope windstorms. *J. Atmos. Sci.*, **36**, 1498–1529.
- , and —, 1983: Nonlinear mountain waves in two and three spatial dimensions. *Quart. J. Roy. Meteor. Soc.*, **109**, 527–548.
- Prusa, J. M., P. K. Smolarkiewicz, and R. R. Garcia, 1996: Propagation and breaking at high altitudes of gravity waves excited by tropospheric forcing. *J. Atmos. Sci.*, **53**, 2186–2216.
- , R. R. Garcia, and P. K. Smolarkiewicz, 1997: Three-dimensional evolution of gravity wave breaking in the mesosphere. Preprints, *11th Conf. on Atmospheric and Oceanic Fluid Dynamics*, Tacoma, WA, Amer. Meteor. Soc., J3–J4.
- Schowalter, D. G., C. W. Van Atta, and J. C. Lasheras, 1994: A study of streamwise vortex structure in a stratified shear flow. *J. Fluid Mech.*, **281**, 247–291.
- Scinocca, J. F., and W. R. Peltier, 1989: Pulsating downslope windstorms. *J. Atmos. Sci.*, **46**, 2885–2914.
- , and —, 1994: Finite-amplitude wave-activity diagnostics for Long's stationary solution. *J. Atmos. Sci.*, **51**, 613–622.
- Smith, R. B., 1985: On severe downslope winds. *J. Atmos. Sci.*, **42**, 2957–2603.
- Smith, S. A., D. C. Fritts, and T. E. VanZandt, 1987: Evidence for a saturated spectrum of atmospheric gravity waves. *J. Atmos. Sci.*, **44**, 1404–1410.
- Smyth, W. D., and W. R. Peltier, 1991: Instability and transition in finite-amplitude Kelvin–Helmholtz and Holmboe waves. *J. Fluid Mech.*, **228**, 387–415.
- , and —, 1993: Two-dimensional turbulence in homogeneous and stratified shear layers. *Geophys. Astrophys. Fluid Dyn.*, **69**, 1–32.
- , and —, 1994: Three-dimensionalization of barotropic vortices on the f-plane. *J. Fluid Mech.*, **265**, 25–64.
- Sonmor, L. J., and G. P. Klaassen, 1997: Toward a unified theory of gravity wave stability. *J. Atmos. Sci.*, **54**, 2655–2680.
- Thorpe, S. A., 1984a: The stability of statically unstable layers. *J. Fluid Mech.*, **260**, 315–331.
- , 1984b: Observations of parametric instability and breaking waves in an oscillating tilted tube. *J. Fluid Mech.*, **261**, 33–45.
- , 1985: Laboratory observations of secondary structures in Kelvin–Helmholtz billows and consequences for ocean mixing. *Geophys. Astrophys. Fluid Dyn.*, **34**, 175–199.
- , 1987: Transitional phenomena and the development of turbulence in stratified fluids: a review. *J. Geophys. Res.*, **92** (C), 5231–5250.
- Voropayev, S. I., Y. D. Afanasyev, and G. J. F. van Heijst, 1993: Experiments on the evolution of gravitational instability of an overturned, initially stably stratified fluid. *Phys. Fluids*, **A5**, 2461–2466.
- Walterscheid, R. L., and G. Schubert, 1990: Nonlinear evolution of an upward propagating gravity wave: Overturning, convection, transience, and turbulence. *J. Atmos. Sci.*, **47**, 101–125.
- Winters, K. B., and J. Riley, 1992: Instability of internal waves near a critical level. *Dyn. Atmos. Oceans*, **16**, 249–278.
- , and E. A. D'Asaro, 1994: Three-dimensional wave breaking near a critical level. *J. Fluid Mech.*, **272**, 255–284.